Combined Sentinel-1A With Sentinel-2A to Estimate Soil Moisture in Farmland

Ying Liu, Jiaxin Qian, and Hui Yue

***Abstract*—In this article, seven filter algorithms were compared. The Lee sigma method was more suitable for estimating soil moisture (SM) than the other filtering methods under different land cover types. First, we used a combination of roughness and the dual-polarized Sentinel-1A backscattering coefficients (VV and VH) to estimate SM in bare soil areas. Second, we employed water cloud model (WCM) to remove the influence of vegetation signals on the land surface backscattering and estimate SM in vegetation-covered areas. SM was also retrieved by modified soil moisture monitoring index (MSMMI) and modified perpendicular drought index (MPDI) of Sentinel-2A images. The results show that MSMMI can more accurately monitor SM in bare soil areas, which was slightly better than synthetic aperture radar (SAR) results. The SAR backscattering coefficients after the removal of vegetation influence by WCM can more precisely estimate SM in vegetation-covered areas, which is significantly better than MSMMI and MPDI, especially in high vegetation-covered areas. Optics and SAR differ in their abilities to estimate SM under different land cover, but the powerful fitting ability of machine learning can make full use of their advantages. We employed the generalized regression neural network (GRNN), support vector regression (SVR), random forest regression (RFR), and deep neural network (DNN) algorithms to estimate SM combining Sentinel-1A with Sentinel-2A images. The estimation accuracies of SM by regression algorithms were higher than those by the semiempirical SAR and optical models. The accuracy of estimated SM by DNN was higher than that of GRNN and RFR, which were better than SVR.**

***Index Terms*—Machine learning (ML) regression, Sentinel-1, Sentinel-2, soil moisture (SM), speckle filter.**

I. Introduction

THE monitoring of soil moisture (SM) on a large scale has always been the focus and difficulty in the world. The traditional SM monitoring methods are mainly carried out by measuring stations or field measurements, which can only obtain a small amount of point data. It is difficult to timely obtain SM distribution in a large area and to reflect the change of SM in space. Remote sensing technique has the advantages of large range, real-time, high efficiency, and low cost, which is the most potent method to quantify SM monitoring [1]. The current monitoring methods of SM are mainly divided into optical and microwave remote sensing. The former includes thermal inertia [2], vegetation water supply index [3], temperature vegetation drought index [4], anomalous vegetation index [5], conditional vegetation index [6], vegetation temperature condition index [7], spectral feature space method [8]–[10], etc. Generally, SM is studied separately in bare soil and vegetation cover areas by microwave. In the aspect of SM estimation in bare soil areas, most researchers established the relationship between synthetic aperture radar (SAR) data and measured surface parameters (root mean square height-s and correlation length-l) to obtain the empirical or semiempirical models. These models, including Oh model [11], Dubois model [12], Shi model [13], and Baghdadi model [14], have certain physical significance and certain statistical laws, which can obtain good precision. Besides, many studies derived the dielectric constant and SM from constructing the mathematical relationship between the backscatter coefficient and surface physical and geometric parameters through the theoretical model of microwave scattering. These theoretical models mainly include the geometrical optics model [15], the physical optics model [16], the small perturbation model (SPM) [17], the integral equation model (IEM) [18], etc. However, these models are too complex to reversely derive the exact expression of SM estimation. The neural network, genetic algorithms, and other optimization algorithms are mostly used to retrieve SM [19]–[21]. The influence of vegetation on radar signal must be eliminated when we adopted these microwave models to evaluate SM in vegetation-covered areas. At present, vegetation scattering model theory, such as Michigan microwave canopy scattering model [22] and Karam model [23], or semiempirical model based on the theoretical model, such as Roo model [24] and WCM (Water cloud model) model [25] are often adopted to eliminate its impacts. The SM will be obtained after get rid of vegetation backscatter from total scatter. The theory of radar remote sensing to estimate SM is rigorous and clear. However, radar signal is greatly affected by surface roughness and vegetation, whose influence is even greater than that of SM. When vegetation is relatively dense, radar signals cannot effectively penetrate vegetation to obtain surface SM signals [18], [26], [27]. At present, the widest estimation methods used SAR data to retrieve SM have mainly changed detection [28], regression analysis [29], and multipolarization method [30].

A major challenge in using SAR to estimate SM is that it is difficult to simulate the complex natural surface with

Manuscript received October 23, 2020; revised November 22, 2020 and November 29, 2020; accepted December 6, 2020. Date of publication December 9, 2020; date of current version January 6, 2021. This work was supported in part by the Natural Science Basic Research Program of Shaanxi under Grant 2020JM-514, in part by the Research on Ecological Restoration and Protection of Coal Base in Arid Eco-fragile Region under Grant GJNY2030XDXM-19-03.2, in part by the project of Shaanxi Coal and Chemical Industry Group under Grant 2018SMHKJ-A-J-03, and in part by the Xi'an University of Science and Technology under Grant 2019YQ3-04 and Grant 2019QDJ024. *(Corresponding authors: Jiaxin Qian; Hui Yue.)*

The authors are with the Xi'an University of Science and Technology, Xi'an 710054, China (e-mail: liuying712100@163.com; 467545659@qq.com; 13720559861@163.com).

Digital Object Identifier 10.1109/JSTARS.2020.3043628

mathematical methods, and precisely measure the two surface roughness parameters (s and l), especially the acquisition of l. Zribi *et al.* (2002) established the empirical relationship between backscattering coefficient difference and a roughness parameter ($Zs = s^2/l$) at different incidence angles (39° and 23°) to assess SM [31]. Baghdadi *et al.* (2006) evaluated the potential of ASAR (advanced synthetic aperture radar) for estimating SM in bare soil. The results show that multi-incidence SAR data can effectively estimate SM, especially at low and high incidence angles, while using two polarizations (HH and HV, horizontal–horizontal and horizontal–vertical) provides little or no improvement over single-polarization (HH or HV) SAR data [32]. However, the multi-incidence angle SAR data is difficult to obtain, and most of the current SAR data are multipolarization combined data. Therefore, it will be of great application value to develop a multipolarization model that can apply to a wide range of incident angles. Yu *et al.* (2010) established an empirical model among the radar backscattering coefficient, SM, and roughness function ($Rs = s^3/l^2$) to monitor SM through the VV (vertical–vertical) and VH (vertical–horizontal) polarization of ASAR data. The results showed that the root mean square error (MSE) between the estimated SM and the measured SM was 0.041 cm^3/cm^3. The model could estimate SM in bare soil areas [33]. This method was employed to assess SM in bare soil areas with the dual-polarization Sentinel-1 data in this article. The WCM was adopted to separate vegetation scattering signals and obtain the surface backscattering coefficient of the land surface, which was applied to estimate SM. Inherent speckle noises reduce image quality and make interpretation of features from SAR images more difficult. The speckle reduction can be achieved by spatial filtering or multilook processing. However, the influence of filtering methods of the backscattering coefficient on SM estimation is rarely discussed in the existing studies. Therefore, this article focused on analyzing the influence of different filtering methods on SM estimation at the pixel scale. Also, modified soil moisture index (MSMMI) and modified perpendicular drought index (MPDI) were obtained by the Sentinel-2A images and compared with SAR results [34], [35].

Optical and SAR data have huge differences in the mechanism of SM estimation, but each has its advantages. The ability to monitor SM is inadequate when SAR or optical data used alone. Many scholars combined them to improve the estimation precision of SM [26], [27], [36]–[38]. Machine learning (ML) regression algorithms have powerful fitting capabilities to better build relationships between different data sources and SM. Therefore, we employed three ML algorithms [the generalized regression neural network (GRNN) [39], the support vector regression (SVR) [40], and the random forest regression (RFR) [41]] and a deep learning (DL) algorithm [the deep neural network (DNN) [42]] to combine Sentinel-1A SAR data with Sentinel-2A optical data in evaluating SM. The estimation results were compared with those obtained from the semiempirical SAR and optical models.

This article mainly explored the following questions.

1) Which backscattering coefficients filtering method is more suitable for dual-polarization Sentinel-1A data to estimate SM under different land cover at the pixel scale?

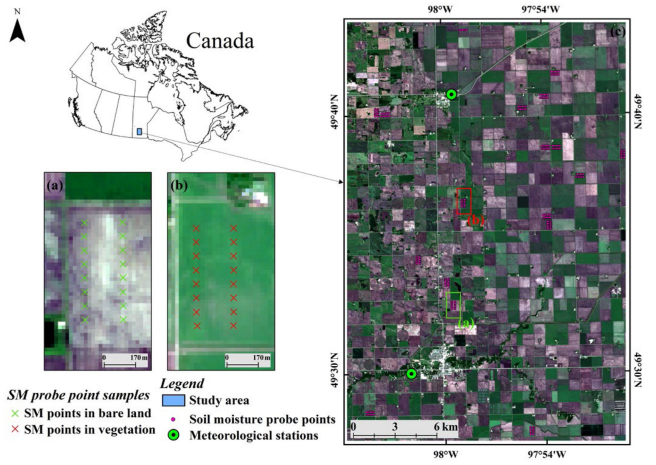

Fig. 1. Geographical location of the study area. (a) SM probe sampling points in bare soil areas. (b) SM probe sampling points in vegetation-covered areas. (c) Sentinel-2 image of the study area on June 13, 2016.

2) What are the similarities and differences in estimating SM using the optical models, the semiempirical dual-polarization SAR models, and the ML regression models?

II. Study Area and Data

The study area locates in Elm Creek and Carman, Manitoba, Canada with an area of 20 × 30 km^2 (Fig. 1). It is a typical temperate continental climate, with hot summer and sunny days, cold and long winter with sufficient sunshine. The terrain of the study area is flat and open. Barley, wheat, canola, soybean, and other cash crops are mainly cultivated in the study area.

The field measured data used in the study were from SMAPVEX16 (Soil Moisture Active Validation Experiment 2016), including the meteorological data, the land cover type data, the measured vegetation status data, the measured fractional vegetation cover (FVC) data, the measured surface roughness data, and the measured SM data [43]–[48]. The dataset is part of passive validation experiments for SM in Carman/Elm, Manitoba, Canada, in 2016. The experiment was designed to calibrate and improve the accuracy of NASA's soil moisture active and passive products [49].

A. Land Cover Map and State of Vegetation Growth

Land cover type data of the study area in 2016 were obtained based on optical satellite images (Landsat8, Sentinel-2, and Gaofen-1) and radar satellite images (Radarsat-2) using the decision tree classification method. The types of land cover include crops (food crops, oil crops, and vegetable crops), woodland, water, bare soil, and cities. The overall accuracy of the dataset with 30 m spatial resolution is more than 85%. This data was mainly used to distinguish between vegetated and nonvegetated areas. The vegetation growth status data mainly includes various plant characteristics of the study area, such as biomass, plant height, plant density, plant water content, and growth stage, which was mainly employed to monitor crop growth status and verify vegetation water content (VWC) estimation results. A total of 23 wheat, 7 oat, 5 corn, 4 canola, 3 soybean, and 1 black

bean samples were measured to obtain VWC on June 13, 2016, all of which were stems and leaves of crops.

B. Filed Measured Vegetation Coverage

FVC data measured the ratio of the projected areas of vegetation coverage to the total projected areas, which was taken by digital photos at the sample points and processed by ViewNX-2 and CanEye5.1 software. The digital photos were taken with a Nikon camera with a fish-eye lens at least 50 cm below the vegetation canopy. There was a total of three sampling points in each field, and at least 10 photos were taken at each sample point. A total of 44 FVC samples were measured on June 13, 2016, including 10 wheat, 12 soybeans (field seeded twice), 9 oats, 5 corn, and 6 canola, ranging from 0.005 to 0.865. The mean and standard deviation of their FVC values are 0.777 ± 0.063, 0.039 ± 0.031, 0.199 ± 0.091, 0.094 ± 0.044, and 0.520 ± 0.130, respectively. This data was mainly used as the verification data of the estimated FVC by Sentinel-2A images on June 13, 2016.

C. Filed Measured Surface Roughness

Surface roughness data included root mean square height (s) and correlation length (l), which were measured using a portable needle profiler 1 m long with 200 red pins. The spacing between each probe was 5 mm. The roughness plate was supported by a pair of brackets and had a mechanism for releasing pins. A retractable metal bar attached to the whiteboard supported the digital camera used to take pictures of roughness contours. A total of 53 roughness samples were measured during June 10 and 15, 2016. The range of s and l are 0.33–1.92 cm and 3.5–32 cm, respectively, and their mean and standard deviation are 0.91 ± 0.34 cm and 13.72 ± 8.05 cm, respectively. This data was mainly used to obtain the empirical coefficients of the SM model by SAR data on June 13, 2016.

D. Field Measured Soil Moisture

The probe-based and the core-based SM data were measured the real dielectric constant (RDC) at a depth of 0–5 cm soil. The collection devices were Stevens Poke and Go. Each probe point measured the top, middle, and bottom of the 0–5 cm soil layer (perpendicular to the top, middle, and bottom of the furrows, respectively). RDC values were converted into volume SM (cm^3/cm^3) using a field-specific calibration equation [48]. The distance between each collection point was at least 70m [Fig. 1(a) and (b)]. All data had been quality-controlled and any erroneous records had been deleted. The Garmin GPS devices were used to locate the sample points when FVC and SM were measured. The accuracy of the GPS was about 3 m. In this article, the average SM of three depths was taken as the measured SM. The air temperature in the study area on the 13th and 14th ranged from 15.5 to 27.5 °C, with a mean and standard deviation of 20.5 and 3.5 °C, respectively. Since there was no measured SM data in the study area on June 13, 2016, and no rain after the 13th, the measured SM data on June 14, 2016, was used as SM verification data. A total of 256 SM samples were measured on June 14, 2016, including 179 bare soil and 77 vegetation sample points. The range of measured SM in bare soil areas and vegetation-covered areas is 0.128–0.459 cm^3/cm^3 and 0.194–0.475 cm^3/cm^3, respectively. Their mean and standard deviations are 0.330 ± 0.074 cm^3/cm^3 and 0.348 ± 0.083 cm^3/cm^3, respectively.

E. Sentinel-1A and Sentinel-2A Data

Sentinel-1A data were obtained from the European Space Agency (ESA). The wide interference pattern is the most commonly used pattern of Sentinel-1, mainly containing two polarization information (VV and VH). The range and azimuth resolutions are 5×20 m, respectively. The Level-1 product contains two kinds of products, i.e., the Single Look Complex (SLC) and the Ground Range Detected (GRD). The SLC products include focused SAR data using satellite orbit and attitude data for geographic reference, which are provided in slant distance mode. The products, with phase and amplitude information, use complete signal bandwidth to achieve single-look processing on each dimension, and complex number to store phase information. Because different filtering algorithms will be compared, GRD products with certain processing were not applied in this article. The path and frame of Sentinel-1A data are 31 and 25–26, respectively. Sentinel-1A data were mainly employed to compare the different backscattering filtering methods and further estimate SM.

Sentinel-2A Level-1C (L1C) data were also obtained from ESA. L1C data are top of atmosphere reflectance products after orthographic correction and geometric accuracy correction of the subpixel level. Atmospheric correction is required to obtain the surface reflectance of each band. The tile numbers of Sentinel-2A are 55 and 14, respectively. Sentinel-2A data were mainly used to obtain vegetation indices, optical SM indices, and FVC.

The dates of remote sensing images and field measured data used in this article are shown in Table I.

III. Methods

The technical flow of this article (Fig. 2) mainly included pretreatment of remote sensing images, comparison of backscattering filtering algorithms, estimation of SM and accuracy verification, etc.

A. Sentinel-1A and Sentinel-2A Preprocessing

The preprocessing of Sentinel-1A mainly contained precision orbit correction, thermal noise removal, radiation calibration, TOPSAR-Deburst, multilook (Range and azimuth looks were set to 4 and 1, respectively), speckle filtering, the slant distance converted to the ground distance (nearest neighbor method), range doppler terrain correction (based on SRTM DEM), radiation normalization, and dB form conversion. Finally, VV and VH backscattering coefficients (σ_{VV} and σ_{VH}) images with different filtering algorithms and 20 m spatial resolution were obtained by the nearest neighbor method.

TABLE I
MEASURED DATA AND REMOTE SENSING DATA INFORMATION USED IN THE STUDY

Images	Satellite acquisition time	Images tile number	Time of field measured data			
			SM	FVC	VWC	Roughness
Sentinel-2A	2016/6/13 11:29	55/14 UNA-UNV	2016/6/14 9:00-11:00	2016/6/13		2016/6/10-15
Sentinel-1A	2016/6/13 11:22	31/25-26				

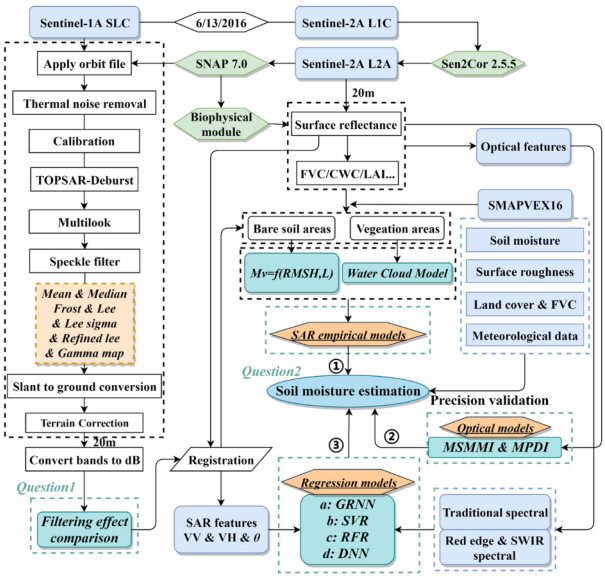

Fig. 2. Technical flowchart.

The Sen2Cor 2.5.5 model was used to generate Sentinel-2A Level-2A (L2A) data. The SNAP 7.0 (Sentinel application platform) software was adopted to obtain 20 m spatial resolution surface reflectance images with average synthesis. The biological quantity module of SNAP was used to obtain FVC, LAI (leaf area index), CWC (canopy water content), CCC (canopy chlorophyll content), and FAPAR (fraction of absorbed photosynthetically active radiation) images. In this module, the PROSPECT+SAIL (scattering by arbitrary inclined leaves) radiation transmission model and artificial neural network (ANN) are used for estimating these parameters [50].

B. Filtering Methods for SAR Backscattering Coefficients

Speckle noise is the main feature which is adapted to distinguish SAR images from optical images. It is related to the imaging mechanism of SAR images [51]. Speckle filtering can be realized by filtering or multilook processing. In this article, seven common filtering methods were selected to explore their influence on estimating SM at pixel scale, including Mean, Median, Frost, Lee, Lee sigma, Refined lee, and Gamma map filter [52]–[59]. The filtering window size of Mean, Median, Frost, Lee, and Gamma map was set to 5 × 5. The filtering window size and sigma value of Lee sigma filter were set to 5 × 5 and 0.9, respectively. The filtering window size of the Refined lee was set to 7 × 7. The Pearson correlation between the filtered backscattering coefficients and the measured probe SM was employed to evaluate the influence of the filtering method on estimating SM. Finally, an appropriate filtering method was selected to further estimate SM by SAR.

C. Soil Moisture Estimation Models by SAR

Generally, SM is estimated in the bare soil areas and vegetation-covered areas, respectively, because the radar echo signal is greatly affected by land cover. The backscattering coefficients of SAR in bare soil areas are mainly related to the surface roughness and the SM content, which can be expressed as [13], [33], [60]:

$$\sigma_{VV}(dB) = g\left(Rs, \theta\right) \cdot f\left(\xi, \theta\right) \tag{1}$$

where $g(Rs, \theta)$ is a function related to roughness and incident angle, $f(\xi, \theta)$is a function related to SM and incident angle.

Under the assumption that the surface autocorrelation function conforms to an exponential distribution if smooth areas and Gaussian distribution if rough areas, the roughness parameters only include s and l [60]–[62]. s and l defined the surface roughness on vertical and horizontal scales, respectively. l is relatively difficult to obtain, but ignoring the influence of l on the backscattering coefficients will bring large errors to the final estimated results of SM [33], [63]–[66]. The roughness function and the SM content function are independent of each other according to (1). Therefore, the AIEM (Advanced IEM) model can be employed to simulate and fix one parameter to analyze the relationship between the other parameter and the backscattering coefficient. Finally, the influence of the two factors (s and l) can be combined to obtain the expressions of the backscattering coefficient and each parameter. Yu *et al.* (2010) employed AIEM to simulate the relationships among backscattering coefficients, SM, s, and l. The results showed that when the incidence angle and SM were fixed, and the range of s and l was set at 0.1–2.0 cm and 2–16 cm, respectively, the following relationship was found by statistical regression:

$$\begin{aligned} \sigma_{\mathrm{VV}}\,(\mathrm{dB}) &= 9.254 \ln(s) - 6.21 \ln(l) + 5.286 \\ \sigma_{\mathrm{VV}}\,(\mathrm{dB}) &\approx 2.98 \ln\left(\frac{s^3}{l^2}\right) + 5.286. \end{aligned} \tag{2}$$

Therefore, if $Rs = s^3/l^2$, a roughness parameter can be subtracted [33]. In the case of specific incident angles and SM, the VV polarization backscattering coefficients in dB scale can be expressed as [33], [67]:

$$\sigma_{\mathrm{VV}}\,(\mathrm{dB}) = E \cdot \ln(Rs) + F \tag{3}$$

where E and F represent empirical coefficients.

The logarithmic relationship could better describe the relationship between σ_{VV} and SM than the linear relationship [33], [68]. Therefore, under the condition of fixed roughness and

incident angle, the expression is as follows:

$$\sigma_{\mathrm{VV}}\,(\mathrm{dB}) = M \cdot \ln(\mathrm{SM}) + N \tag{4}$$

where *M* and *N* represent empirical coefficients.

Therefore, when the radar incident angle is constant, the expression of the backscattering coefficients can be expressed as follows by combining (3)–(4) [33]:

$$\sigma_{\mathrm{VV}}\,(\mathrm{dB}) = (E\ln(Rs) + F) \cdot (M\ln(\mathrm{SM}) + N) \tag{5}$$

which can be written as

$$\sigma_{\mathrm{VV}}\,(\mathrm{dB}) = a\ln(Rs) + b\ln(\mathrm{SM}) + c\ln(Rs)\ln(\mathrm{SM}) + d \tag{6}$$

where the empirical coefficients *a*, *b*, *c,* and *d* can be obtained by the least square method (LS) according to the measured SM, the measured surface roughness, and the backscattering coefficients of SAR images.

The VH polarization backscattering coefficient also has a similar relationship with *SM* and *Rs*, that is [33]

$$\sigma_{\mathrm{VH}}\,(\mathrm{dB}) = e\ln(Rs) + f\ln(\mathrm{SM}) + g\ln(Rs)\ln(\mathrm{SM}) + h \tag{7}$$

where *e*, *f*, *g,* and *h* also can be obtained by LS according to the measured SM, the measured surface roughness, and the backscattering coefficients of SAR images.

Rs can be offset and SM can be further obtained by the simultaneous (6)–(7). Let $\ln(Rs)$ be *X* and $\ln(\mathrm{SM})$ be *Y*. The specific derivation is as follows:

$$\begin{cases} \sigma_{\mathrm{VV}}\,(\mathrm{dB}) = aX + bY + cXY + d \\ \sigma_{\mathrm{VH}}\,(\mathrm{dB}) = eX + fY + gXY + h \end{cases}$$

$$\begin{cases} g\sigma_{\mathrm{VV}} = gaX + gbY + gcXY + gd \\ c\sigma_{\mathrm{VH}} = ceX + cfY + cgXY + ch \end{cases}$$

$$g\sigma_{\mathrm{VV}} - c\sigma_{\mathrm{VH}} = (ga - ce)\,X + (gb - cf)\,Y + (gd - ch)$$

$$X = \frac{gb - cf}{ce - ga}Y + \frac{gd - ch}{ce - ga} + \frac{c\sigma_{\mathrm{VH}} - g\sigma_{\mathrm{VV}}}{ce - ga} = \Delta$$

$$\sigma_{\mathrm{VV}} = a\Delta + bY + c\Delta Y + d$$

$$= \frac{agb - acf}{ce - ga}Y + \frac{agd - ach}{ce - ga} + \frac{ac\sigma_{\mathrm{VH}} - ag\sigma_{\mathrm{VV}}}{ce - ga} + bY$$

$$+ \frac{cgb - c^2 f}{ce - ga}Y^2 + \frac{cgd - c^2 h}{ce - ga}Y + \frac{c^2\sigma_{\mathrm{VH}} - cg\sigma_{\mathrm{VV}}}{ce - ga}Y + d$$

$$\begin{pmatrix} cgb \\ -c^2 f \end{pmatrix} Y^2 + \begin{pmatrix} agb - acf + bce + bga \\ +cgd - c^2 h + c^2\sigma_{\mathrm{VH}} - cg\sigma_{\mathrm{VV}} \end{pmatrix} Y$$

$$+ \begin{pmatrix} ga \\ -ce \end{pmatrix} \sigma_{\mathrm{VV}} = 0. \tag{8}$$

By derivation of (8), *X* (i.e., *Rs*) is eliminated. The backscattering coefficients of VV and VH polarization are known in SAR images. Therefore, *Y* (i.e., SM) can be derived by solving the quadratic equation of one variable.

SAR signals in vegetation-covered areas are affected by vegetation, so it is difficult to directly estimate SM by backscattering coefficients. Attema and Ulaby put forward the classic WCM based on the radiative transfer theory, mainly for crop covered [25]. The model assumes that the vegetation layer is composed of many evenly distributed scattered particles of the same size and shape, and the multiple scattering of vegetation and surface soil can be ignored. The expressions are as follows:

$$\begin{aligned} \sigma^0 &= \sigma^0_{\mathrm{veg}} + \gamma^2\sigma^0_{\mathrm{soil}} \\ \sigma^0_{\mathrm{veg}} &= A \times \cos(\theta) \times \left(1 - \gamma^2\right) \\ \gamma^2 &= \exp\left(-2 \times B \times \mathrm{VWC} \times \sec\theta\right) \end{aligned} \tag{9}$$

where σ^0 is the backscattering coefficient scattered by vegetation layer, σ^0_{veg} is the backscattering coefficient of vegetation, σ^0_{soil} is the soil surface backscattering after double-path attenuation by vegetation layer, γ^2 is the double-layer attenuation factor (transmittance) of radar wave penetrating vegetation layer. The values of A and B are dependent on the frequency of vegetation types and incidence angle, θ is the radar incidence angle, and *VWC* is VWC.

Accurate estimation of VWC is the key to separate vegetation signals from total backscattering coefficients of SAR by WCM. Different CWC indices were compared with measured VWC data in this article, which including MSI (moisture stress index), MSI2, SRWI (simple ratio water index), NDMI (normalized difference moisture index), njormalized difference vegetation Index, NMDI (normalized multiband drought index) [69]–[74], and vegetation biomass indices (CCC, CWC, FAPAR, FVC, and LAI) obtained by SNAP. Their equations are as follows:

$$\begin{aligned} \mathrm{MSI} &= R_{\mathrm{SWIR1}}/R_{\mathrm{NIR}};\ \mathrm{MSI}_2 = R_{\mathrm{SWIR2}}/R_{\mathrm{NIR}} \\ \mathrm{SRWI} &= R_{\mathrm{NIR}}/R_{\mathrm{red}};\ \mathrm{NDVI} = \frac{R_{\mathrm{NIR}} - R_{\mathrm{red}}}{R_{\mathrm{NIR}} + R_{\mathrm{red}}} \\ \mathrm{NDMI} &= \frac{R_{\mathrm{NIR}} - R_{\mathrm{SWIR1}}}{R_{\mathrm{NIR}} + R_{\mathrm{SWIR1}}}; \\ \mathrm{NMDI} &= \frac{R_{\mathrm{NIR}} - R_{\mathrm{SWIR1}} + R_{\mathrm{SWIR2}}}{R_{\mathrm{NIR}} + R_{\mathrm{SWIR1}} - R_{\mathrm{SWIR2}}} \end{aligned} \tag{10}$$

where R_{red}, R_{NIR}, R_{SWIR1}, and R_{SWIR2} represent the reflectance of Red, NIR (near-infrared), SWIR1 (short-wave infrared1), and SWIR2 (short-wave infrared2) of Sentinel-2, respectively.

D. Soil Moisture Estimation Models From Optical Images

The MPDI and the MSMMI from Sentinel-2A images were selected to retrieve SM, and compared with results by SAR models. In the NIR-red feature space, the dryness of any point is determined by PDI and perpendicular vegetation index. The smaller the SM is, the farther the pixel is from the coordinate's origin. The larger the MPDI value is, the more serious the dryness is [34]. The acquisition of the soil line is easily affected by soil texture and land cover, which further affects the accuracy of SM estimation from MPDI. MSMMI reflects the wetness and dryness condition of the pixel which does not need soil lines [35]. Studies have shown that NIR-red space could not effectively reflect SM in vegetation-covered areas [74], [75]. The SWIR band is a strong absorption band of water, which has been proved to more effectively estimate surface SM. The SWIR1–SWIR2

feature space was adopted to replace the NIR-red space of MPDI and MSMMI. The expressions are as follows:

$$\mathrm{MPDI} = \frac{R_{\mathrm{SWIR1}} + M \cdot R_{\mathrm{SWIR2}} - \mathrm{FVC}\left(R_{v,\mathrm{SWIR1}} + M \cdot R_{v,\mathrm{SWIR2}}\right)}{(1-\mathrm{FVC})\sqrt{M^2+1}} \tag{11}$$

$$\mathrm{MSMMI} = \frac{\sqrt{\left(R_{\mathrm{SWIR1}} - \mathrm{FVC} \cdot R_{v,\mathrm{SWIR1}}\right)^2 + \left(R_{\mathrm{SWIR2}} - \mathrm{FVC} \cdot R_{v,\mathrm{SWIR2}}\right)^2}}{\sqrt{2}\,(1-\mathrm{FVC})} \tag{12}$$

where M is the slope of the soil line obtained through interactive data language. FVC is vegetation coverage obtained by SNAP. $R_{v,\ \mathrm{SWIR1},}$ and $R_{v,\ \mathrm{SWIR2}}$ is the reflectance of SWIR1 and SWIR2 bands of pure vegetation (FVC > 0.9).

E. Machine Learning Regression Models

The physical mechanisms of SM estimation by optical and SAR remote sensing are completely different, but there are close relationships between them, which it is difficult to establish relationships between them directly by the strict mathematical expression [76]. ML regression algorithms are often applied to estimate many remote sensing parameters (such as biomass) due to strong nonlinear fitting characteristics [77]. In this article, the performance of three traditional ML and a DL regression models for estimating SM was compared.

The GRNN is an improvement based on radial basis function [78], and its theoretical basis is nonlinear regression analysis [39]. GRNN has strong nonlinear mapping ability and learning speed, and its network finally converges to the optimization regression with more sample size clustering. When the sample data is small, the prediction effect is very good. The network can also handle unstable data. In this article, a five-fold cross-validation method was used to automatically find the optimal parameters of GRNN between the training sets and test sets with the minimum MSE and further estimated SM.

The support vector machine (SVM) is an algorithm used for classification (SVC) and can also be used for regression, namely the SVR [40]. At present, SVR is widely used in the estimation of remote sensing quantitative parameters such as LAI, SM, and FVC [79]–[81]. The difference between SVR and SVC is that the sample points of SVR end up with only one category. The optimal hyperplane it seeks is not to separate two or more sample points as SVM does, but to minimize the total deviation of all sample points from the hyperplane. The Linear and Gaussian kernel function were used in this article. The FitrSVM was used to automatically optimize the hyperparameters (with the minimum MSE) through five-fold cross-validation and further estimated SM.

The random forest (RF), as a relatively new ML model, can well predict the effects of up to thousands of explanatory variables and is regarded as one of the best ML algorithms [41]. The RFR algorithm is mainly applied to the estimation of yield, vegetation biomass, LAI, and SM [82]–[85]. RF is composed of multiple decision trees, and there is no correlation between each decision tree in the forest. When dealing with the regression problem, the prediction result of RFR is obtained from the average value of all the prediction results of the internal decision tree. The importance of features in the RF indicates the degree of influence of features on the prediction results, which is determined by the average value of all internal decision trees. In this article, the number of RFR decision trees was set as 200, and the maximum characteristic number mode was set as a square root.

TABLE II
FEATURES USED FOR SOIL MOISTURE ESTIMATION

Groups	Features
a (11)	***Traditional spectrum:*** Blue, Green, Red, NIR, and Narrow-NIR (nNIR); SRWI [69], NDVI [68], Differential vegetation index (DVI) [88], Enhanced vegetation index (EVI) [89], Modified soil adjusted vegetation index (MSAVI) [90], and Carotenoid Reflectance Index1 (CRI1) [91].
b (44)	*All optical data:* ***Traditional spectrum (Group a)*** ***& Red edge spectrum:*** Red edge1/2/3, Anthocyanin Reflectance Index 1/2 (ARI1/2) and Carotenoid Reflectance Index2 (CRI2) [91],[92], NDre1/2/3, NDVIre21/31/32, Modified red edge normalized difference vegetation index (MRENDVI) [93],[94], Modified red edge simple ratio (MRESR) [93],[94], Red edge position index of Sentinel-2 (S2REP) [95], Triangular vegetation index (TVI) [96], Novel inverted red-edge chlorophyll index (IRECI) [97], Terrestrial chlorophyll index (MTCI) [98], Red edge chlorophyll index ($\mathrm{CI}_{\mathrm{red\ edge}}$) [99], Modified chlorophyll absorption ratio index (MCARI and MCARI2) [100],[101] and Transformed chlorophyll absorption reflectance index (TCARI) [100]. ***& Short-wave infrared spectrum:*** SWIR1/2, MSI [70], MSI2 [73], NDMI [71] and NMDI [72]. ***& Biomass features:*** FVC, LAI, CCC, CWC, and FAPAR
c (5)	SAR data: VV, VH, VV-VH, VV/VH, θ
d (16)	SAR data & Traditional spectrum of optics (Group a)
e (49)	SAR & all-optical data (Group b)

The DNN is an improvement of the multilayer perceptron [86], [87], which employs ReLU or Maxout transmission function to replace the Sigmoid function to overcome the gradient disappearance. Structurally, there is no difference between a fully connected DNN and a multilayer perceptron. Since the maximum number of feature variables involved in regression in this article was 49 (Table II), DNN regression analysis was performed for all feature variables. The number of input and output layers of DNN was set as 49 and 1, respectively. The hidden layer was set as 49. The initial learning rate of DNN was set as 0.01, the maximum number of single iterations was set as 500, the activation function was set as ReLU, and the loss function was set as MSE loss function. The early stop method was used to prevent overfitting by limiting the number of iterations (20 times at a time). If the error of training samples decreased and the test samples' accuracy did not improve, then early stop command will be executed.

F. Selection of Machine Learning Regression Features

The feature groups used for ML regression are shown in Table II. Group (a) contains the traditional spectral features

(blue, green, red, NIR, and narrow-NIR) and corresponding vegetation indices. Group (b) added red edge bands (red edge1, red edge2, and red edge3), SWIR bands (SWIR1 and SWIR2), corresponding vegetation indices, and vegetation biomass features obtained by SNAP (FVC, CWC, CCC, LAI, and FAPAR). Group (c) contains SAR features (VV, VH, and radar incident angle). Group (d) is a combination of Group (a) and Group (c). Group (e) is a combination of Group (b) and Group (c). Replace red band in NDVI with three red edge bands of Sentinel-2, and obtain NDre1, NDre2, and NDre3. Replace red and NIR bands in NDVI with red egde2 and red egde1 bands, respectively, and obtain NDVIre21. In the same way, NDVIre31 and NDVIre32 were obtained. If the central wavelength of the formulae in Table II could not be obtained in Sentinel-2, the nearest reflectance band was used instead.

G. Accuracy Validation

In this article, there were 256 samples of measured SM, including 179 samples in bare soil areas and 77 samples in vegetation-covered areas. The measured SM sample points were sorted according to the corresponding FVC value estimated by SNAP. A total of 86 samples (about 1/3 of all samples) were selected for verification at intervals of 2. The remaining samples (a total of 170) were training samples for modeling. The R (Pearson correlation coefficient), MAE (mean absolute error), MRE (mean relative error), and RMSE (root mean square error) were used to evaluate the accuracy of each SM estimation model. The calculation formulae of the accuracy indices are as follows:

$$R = \frac{\mathrm{Cov}\,(X, Y)}{\sqrt{\mathrm{Var}\,(X)\,\mathrm{Var}\,(Y)}}$$

$$\mathrm{MAE} = \frac{1}{n} \cdot \sum_{i=1}^{n} |X_{obs,i} - X_{\mathrm{mod}\,el,i}|$$

$$\mathrm{MRE} = \frac{1}{n} \cdot \sum_{i=1}^{n} \frac{|X_{obs,i} - X_{\mathrm{mod}\,el,i}|}{X_{obs,i}}$$

$$\mathrm{RMSE} = \sqrt{\frac{\sum_{i=1}^{n} \left(X_{obs,i} - X_{\mathrm{mod}\,el,i}\right)^2}{n}} \tag{13}$$

where X represents estimated SM, Y represents measured SM, Cov(X,Y) represents the covariance of X and Y, Var(X) and Var(Y) represents the variance of X and Y, n represents the total number of validation data, $X_{obs,i}$ represents the ith value of measured SM, $X_{\mathrm{model},i}$ represents the ith value of estimated SM.

We can see from Fig. 3, on the whole, the MAE, MRE, and RMSE of estimated FVC by SNAP are 0.062, 9.977%, and 0.079, respectively. The MAE, MRE, and RMSE of estimated LAI by SNAP are 0.443, 9.078%, and 0.707, respectively. Therefore, the vegetation biomass indices derived from the Sentinel-2 L2A product can effectively represent the actual vegetation coverage in the study area, but the estimated LAI is significantly underestimated. The FVC in the study area was complex and the growth of crops varied. $0 \leq \mathrm{FVC} < 0.30$ and $0.30 \leq \mathrm{FVC} < 0.45$ were considered as the non-vegetation and the low vegetation-covered areas, respectively. $0.45 \leq \mathrm{FVC} < 0.60$ and

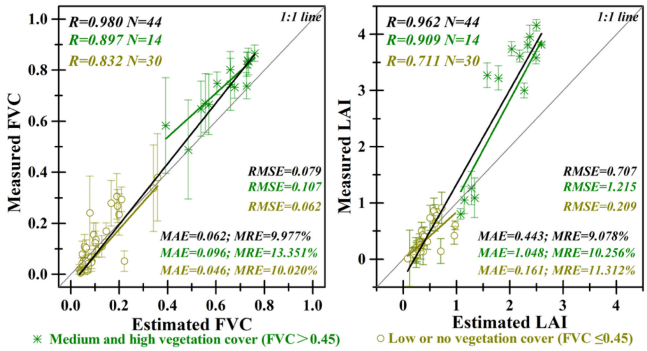

Fig. 3. Comparison between the estimated FVC and LAI by SNAP and corresponding measured data.

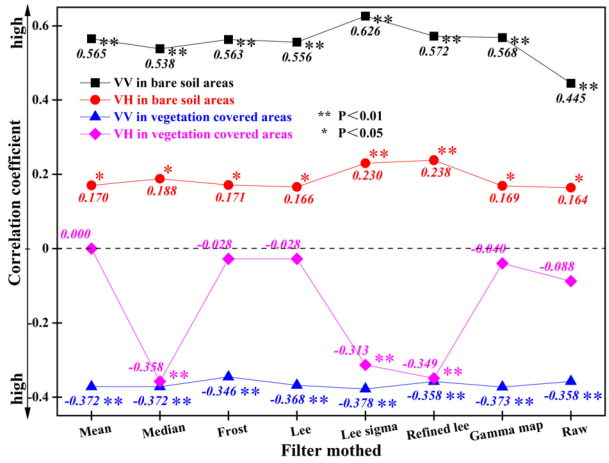

Fig. 4. Correlation between backscatter coefficients after different filtering algorithms and measured SM.

FVC $\geq$ 0.60 were regarded as the medium vegetation and the high vegetation-covered areas, respectively [102].

IV. Results

A. Analysis of Different SAR Backscattering Filtering Methods

The measured SM in different land cover types was adopted to illustrate the performance of each filtering method. Fig. 4 indicates that R between σ_{VV} and measured SM in bare soil areas of each filtering method is higher than that of σ_{VH}. The highest and the lowest is σ_{VV} after Lee sigma filtering ($R = 0.626$) and the original unfiltered imagery ($R = 0.445$), respectively. Only Refined Lee filter and Lee sigma filter of σ_{VH} pass 99% significance test ($R = 0.238$ and 0.230, respectively). σ_{VV} in vegetation-covered areas of each filtering method is negatively correlated with measured SM ($P < 0.01$). R differs little and the highest is the Lee sigma filter ($R = -0.378$). R between σ_{VH} and measured SM is significantly lower than that of σ_{VV}. Median, Lee sigma, and Refined Lee filtering methods pass 99% significance test, but R is low. This is due to the strong penetration of VV polarization which is still affected by signals such as VWC. VH polarization has a strong depolarization effect in vegetation-covered areas, which is mainly affected by vegetation

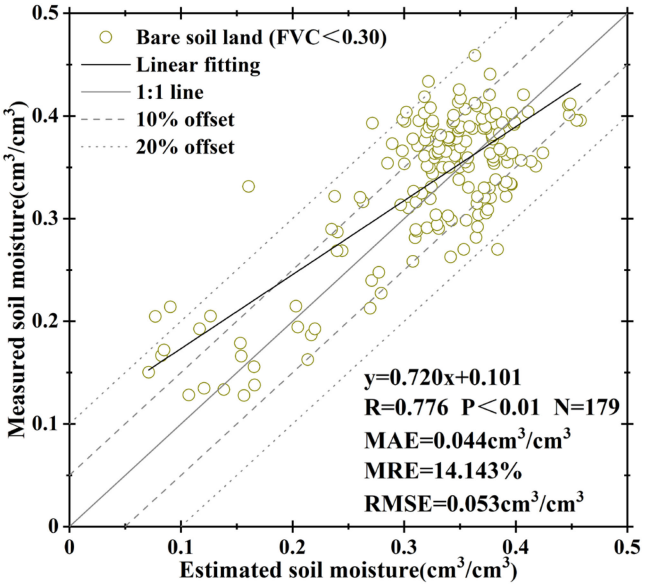

Fig. 5. Relationship between estimated SM and measured SM in bare soil areas.

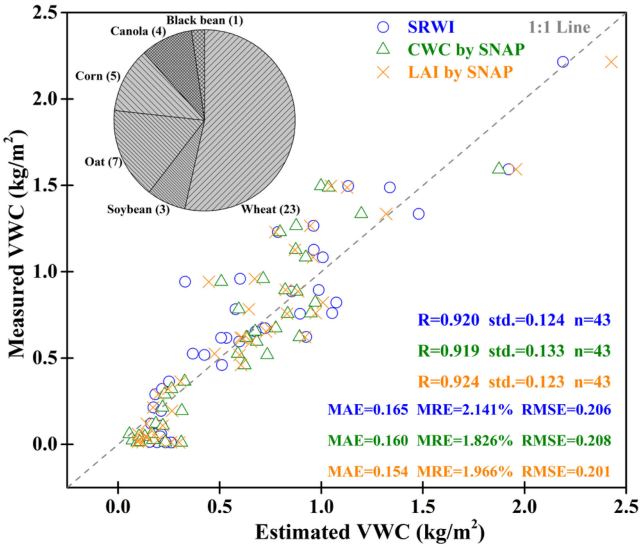

Fig. 6. Comparison between estimated VWC and measured VWC.

scattering. Therefore, other auxiliary data must be applied to eliminate the impact of vegetation cover on the backscattering coefficients when the study area is covered with vegetation. The above analysis shows that the Lee sigma filtering algorithm is the best filtering method to estimate SM using backscattering coefficients of Sentinel-1.

In the Lee sigma algorithm, the number of iterations (k) has great influences on the final filtering results. In this article, the target window was set as 3×3, the filtering window as 5×5, the k value as 1, 2, and 3, and the sigma value as 0.9. The results show that when k increases, R between σ_{VV} and measured SM in bare soil areas decreases, while R in vegetation-covered areas remains unchanged. R between σ_{VH} and measured bare soil and vegetation-covered SM increased gradually, but the improvement is small. Therefore, k in the Lee sigma filter method was set as 1 to meet the requirements for estimating SM.

B. Estimation of Soil Moisture by SAR Empirical Models

According to (6) and (7) of the empirical SAR model, the combined roughness (Rs) by field measurement, the measured SM and the Sentinel-1 dual-polarization backscattering coefficients after Lee sigma filter method were directly introduced to obtain empirical coefficients a-h of (6) and (7). The empirical models of equations were

$$\sigma_{\mathrm{VV}}\,(\mathrm{dB}) = -2.144\ln(R_s) - 14.039\ln(m_v) - 2.610\ln(R_s)\ln(m_v) - 19.349 \quad (14)$$

$$\sigma_{\mathrm{VH}}\,(\mathrm{dB}) = 2.205\ln(R_s) + 10.370\ln(m_v) + 1.759\ln(R_s)\ln(m_v) - 4.585. \quad (15)$$

By combining (14) and (15), SM can be derived after offsetting the roughness. Fig. 5 demonstrates that R between estimated SM from dual-polarization backscattering coefficients and measured SM is 0.776. The corresponding MAE, MRE, and RMSE are 0.044 $\mathrm{cm}^3/\mathrm{cm}^3$, 14.143%, and 0.053 $\mathrm{cm}^3/\mathrm{cm}^3$, respectively. Most points are within the bias range of 10%, and few points are outside the bias range of 20%, which may be affected by the surface roughness or SAR speckle noise. The above results show that the semiempirical model with combined roughness (Rs) can effectively monitor SM in bare soil areas in the study area.

Estimated VWC is the key to precisely separate vegetation signals from the backscattering of the surface soil by WCM. Compared with measured VWC on June 13, 2016, we found that MSI, MSI2, and NMDI have obvious power relationships with measured VWC (R is 0.890, 0.875, and 0.872, respectively). NDVI and NDMI have an obvious exponential relationship with measured VWC (R is 0.836 and 0.892, respectively), and SRWI has an obvious linear relationship with measured VWC ($R = 0.920$). There is also a significant linear relationship between CCC, CWC, FAPAR, FVC, LAI, and measured VWC (R is 0.878, 0.919, 0.906, 0.911, and 0.924, respectively). The above results show that SRWI, CWC, and LAI are highly correlated with measured VWC. Fig. 6 indicates that the scatter points of estimated VWC (from SRWI, CWC, and LAI) and measured data are uniformly distributed on both sides of the 1:1 trend line. The estimation accuracy of the three indices is almost the same. As LAI has the lowest MAE and RMSE and has a good correlation with the measured LAI (Fig. 3), it was adopted to estimate VWC in the WCM. The VWC equation is as follows:

$$\mathrm{VWC} = 0.396 \cdot \mathrm{LAI} + 0.020. \quad (16)$$

Due to rich types of vegetation cover in the study area, the coefficients A and B in the WCM were set to 0.0012 and 0.091, respectively [23]. Therefore, backscattering coefficients of surface soil in the vegetation-covered areas after WCM can

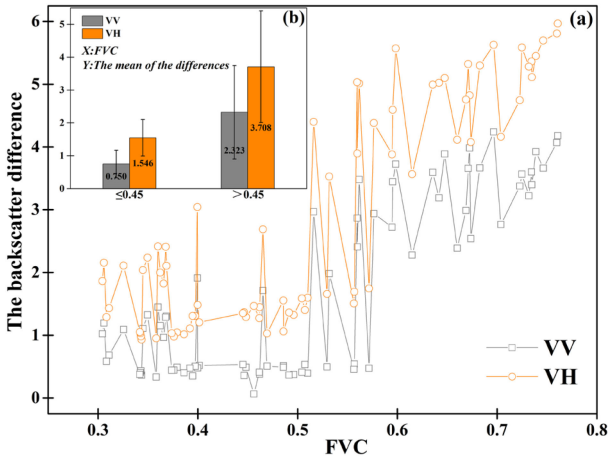

Fig. 7. (a) Difference between different polarization backscattering coefficients before and after removal of vegetation under different FVC conditions. (b) Average difference between the backscattering coefficients under FVC $\leq$ 0.45 and FVC $>$ 0.45.

be further expressed as

$$\sigma^0_{\text{soil}} = \frac{\sigma^0 - 0.0012\cos(\theta)}{\exp\left[-2\cdot 0.091\left(0.396\cdot \text{LAI} + 0.020\right)\cdot \sec(\theta)\right]} + 0.0012\cos(\theta) \tag{17}$$

where σ^0_{soil} is the soil backscattering coefficient after removing the influence of vegetation, σ^0 is the total backscattering coefficient of the vegetation layer, LAI represents the LAI obtained by SNAP, θ represents the radar incident angle.

Fig. 7 shows that σ_{VV} have no significant difference before and after vegetation correction in $0.3 < \text{FVC} \leq 0.45$. The variation ranges from 0.5 to 1.5 dB. While the difference is obvious in FVC $>$ 0.45 which ranges from 1.0 to 4.0 dB. σ_{VH} has a significant difference before and after correction in $0.3 < \text{FVC} \leq 0.45$, ranging from 1.0 to 3.0 dB, which ranges from 1.5 to 6.0 dB in FVC $>$ 0.45. The difference between σ_{VH} before and after correction is significantly greater than that of σ_{VV} under the same FVC condition. When FVC $\leq$ 0.45, the average difference σ_{VV} andσ_{VH} is 0.75 and 1.55 dB, respectively. When FVC $>$ 0.45, the average difference of σ_{VV} is 2.32 dB, while σ_{VH} is 3.71 dB. The copolarized backscattering has good penetrability and is less relatively affected by VWC. However, cross-polarization mainly reflects the scattering signal of vegetation. The backscattering coefficient before and after removing the influence of vegetation by WCM is quite different, especially in the areas with medium and high vegetation coverage.

Fig. 8 shows that there is a significant negative correlation ($P < 0.01$) among σ_{VV}, σ_{VH} and measured SM after removing vegetation influences by WCM. Compared with the vegetation signals not removed (Fig. 4), R between backscattering coefficients and measured SM was increased after vegetation correction. R between σ_{VV} and measured SM in the whole vegetation-covered areas is -0.828, while it is -0.886 between σ_{VH} and measured SM. R between σ_{VV} and measured SM in the wheat field is -0.602 ($P < 0.01$), which is low in the canola field ($P > 0.01$). R between σ_{VH} and measured SM in

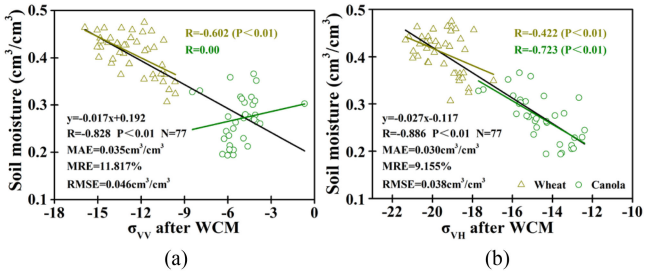

Fig. 8. Relationships between backscattering coefficients of VV (a) and VH (b) and measured SM after removal of vegetation by WCM.

the wheat field is -0.422 ($P < 0.01$), which is -0.723 ($P < 0.01$) in the canola field. This indicates that VV polarization of Sentinel-1 can better describe the SM in the wheat field, while VH polarization can more precisely describe the SM in the canola field. The average FVC of the whole crop was 0.510 ($\pm$0.138, STD). The average FVC of wheat and canola were 0.572 ($\pm$0.149) and 0.433 ($\pm$0.071), respectively. The wheat was in the stage of three-leaf unfolding, which required a lot of water. Most canola was in the early stage of growth, with a small root amount, few leaves, small transpiration area, and relatively small water demand. Therefore, SM in the wheat field was relatively higher than that of canola. This further proves that backscattering coefficients after removing vegetation influence by WCM can precisely estimate SM in vegetation-covered areas. VH polarization could more precisely assess the overall SM conditions in this period in the study area.

C. Comparison Between SAR Models and Optical Models

In part B of the Results section, Sentinel-1 data was employed to separately estimate SM in bare soil areas and vegetation-covered areas. This section mainly compares the similarities and differences between optical models (MSMMI and MPDI by Sentinel-2) and SAR models in estimating SM under different land cover types. There are significant negative linear correlations between MSMMI and MPDI from the SWIR1-SWIR2 feature space and measured SM. Fig. 9 demonstrates that R between estimated SM by VH polarization and measured SM is the highest ($R = 0.807$), followed by VV polarization ($R = 0.787$). R between estimated SM by MSMMI and measured SM is 0.710, which is higher than that from MPDI ($R = 0.550$). R between estimated SM by SAR and measured SM in bare soil areas (FVC < 0.30) is 0.776, slightly higher than MPDI ($R = 0.770$), which significantly lower than MSMMI ($R = 0.837$). The estimation results by SAR are better than MSMMI and MPDI in vegetation-covered areas. We can see from Fig. 10 that, when $0.30 \leq \text{FVC} < 0.60$, estimation accuracy of VH polarization is the highest, which is slightly better than VV polarization, significantly better than MSMMI and MPDI. When FVC $>$ 0.60, estimation accuracy of VV polarization is the highest, which is slightly better than VH polarization, also significantly better than MPDI and MSMMI. The above results show that the estimation accuracy of SM from MSMMI in bare soil areas is slightly higher than that of SAR, which is significantly higher

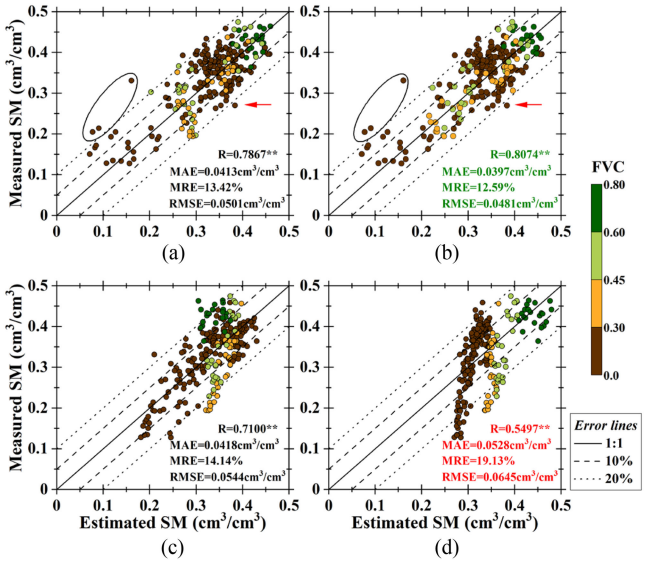

Fig. 9. Scatter diagrams of estimated SM and measured SM. (a), (b), estimated SM in bare soil areas (FVC < 0.30) by VV and VH polarization, and estimated SM in vegetation-covered areas (FVC ≥ 0.30) by WCM, respectively. (c), (d), estimated SM by MSMMI and MPDI from SWIR1–SWIR2 space, respectively.

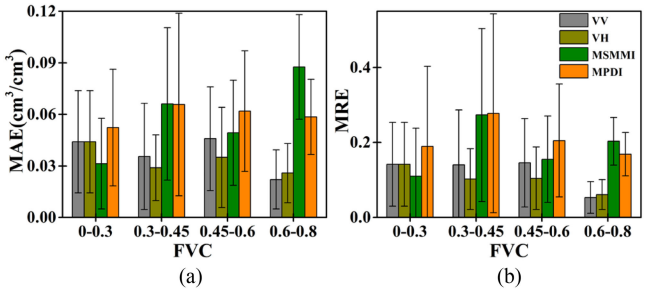

Fig. 10. Estimated accuracy of SM by each index under different vegetation coverage (the error line represents the standard deviation).

than that of MPDI. The semiempirical model based on VV and VH backscattering coefficients can reflect the SM in bare soil areas to a certain extent. σ_{VV} and σ_{VH} after removing vegetation influence by WCM can precisely monitor SM status in vegetation-covered areas, which is higher than that of optical SM models. The estimation accuracy of MSMMI was significantly higher than that of MPDI in middle and low vegetation-covered areas, while lower than that of MPDI in high vegetation-covered areas. Fig. 9(d) indicates that the scatter points of estimated SM and measured SM by MPDI under different FVC are stratified, which is the reason why the overall estimation accuracy is low.

Fig. 11 expresses that the spatial distribution of SM estimated by SAR is generally consistent with that from the optical SM index (MSMMI). As shown in Fig. 12, the histogram of estimated SM by SAR images presents a standard Gaussian distribution. Estimation results by optical images are also Gaussian, but there is a small uplift in the SM high-value region. The mean and standard deviation of estimated SM by SAR and optical images are 0.3753 ± 0.1016 cm^3/cm^3 and 0.3427 ± 0.0662 cm^3/cm^3, respectively. Estimated SM by SAR which greater

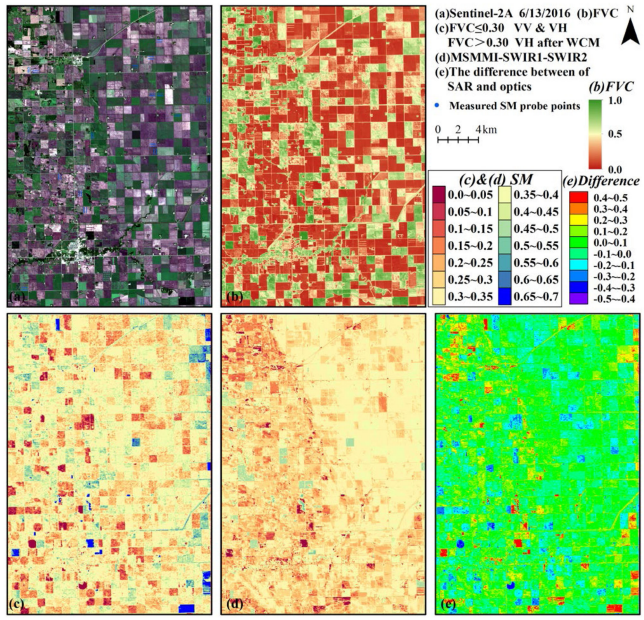

Fig. 11. SM spatial distribution maps are estimated by optical images and SAR images on June 13, 2016. (a) Sentinel-2A imagery. (b) FVC. (c) Estimated SM by SAR images on June 13, 2016 (SM in bare soil areas was estimated by VV and VH polarization, and which in vegetation areas was estimated by VH polarization and WCM model). (d) Estimated SM by MSMMI on June 13, 2016. (e) Difference of estimated SM between SAR images and optical images (the former minus the latter).

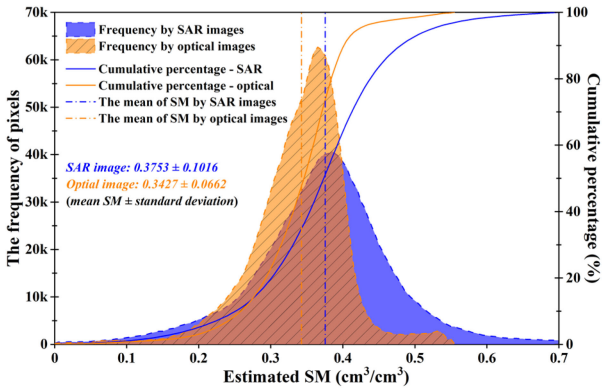

Fig. 12. Histogram of estimated SM by SAR and optical images.

than 0.4 cm^3/cm^3 and 0.45 cm^3/cm^3 accounted for about 36% and 17%, respectively, while the optical estimation results are only about 11% and 3%, respectively. Fig. 11(c) shows that the estimated SM by SAR in bare soil areas was relatively low, which was high in the vegetation-covered areas. The saturated water was mainly located in the water areas and part of vegetation-covered areas. Fig. 11(d) indicates that areas with low SM estimated by MSMMI were mainly located in the bare soil areas and part of vegetation-covered areas in the northwest region, while areas with relatively high SM were mainly located in vegetation cover areas. Fig. 11(e) illustrates that the difference between estimated SM by SAR and by optics at 0.0–0.1cm^3/cm^3

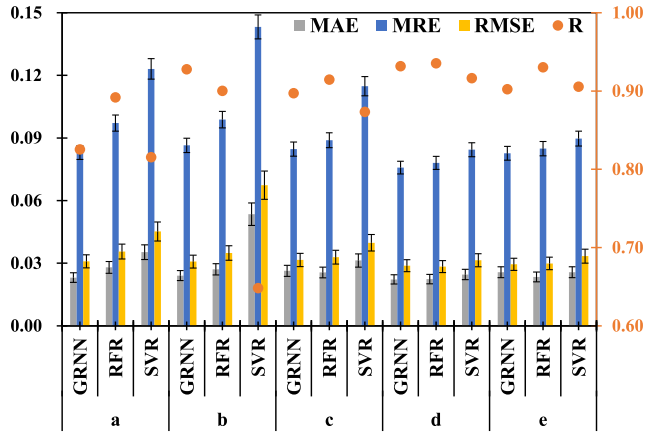

Fig. 13. Accuracy of estimated SM by different traditional machine learning regression algorithms.

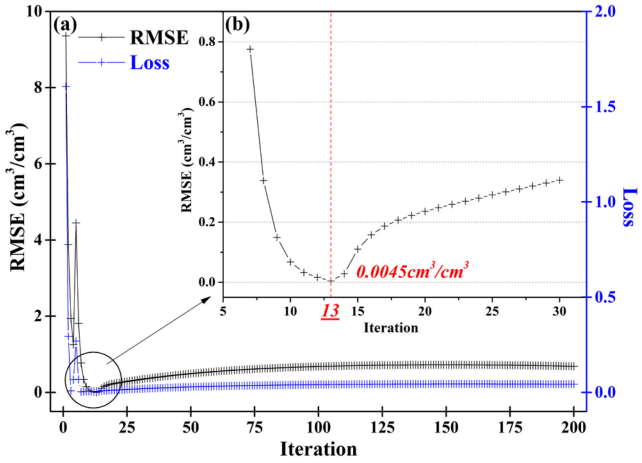

Fig. 14. Relationships between the number of iterations and estimation accuracy of SM by DNN (loss is the result of MSE loss function).

and -0.1–0.0 cm^3/cm^3 accounts for about 29% and 38%, respectively. The proportion of difference at 0.1–0.2 cm^3/cm^3 was about 7.72%, and >0.2 cm^3/cm^3 was about 2.32%. The proportion of difference at -0.2–-0.1cm^3/cm^3 accounted for about 15.79%, and <-0.2 cm^3/cm^3 accounted for about 6.15%. The areas with a positive difference of SM were mainly located in a small part of bare soil areas in the northwest of the study area and vegetation-covered areas (mainly wheat). The areas with negative SM difference were were mainly located in the bare soil areas in the middle of the study area. The proportion of estimated SM by SAR images higher than that by MSMMI was 39.04%, which was mainly located in the vegetation-covered areas. Its spatial distribution is highly consistent with the middle and high vegetation-covered areas in the study area (the proportion of FVC ≥ 0.45 was about 34.58%). Combined with field measured data [Fig. 9(c)], we can find that MSMMI significantly underestimated SM in high vegetation-covered areas, mainly because optical images mainly reflected vegetation canopy information and can only indirectly reflected the dryness and wetness conditions of vegetation underlie. SAR images were greatly affected by surface roughness and other factors and may overestimate or underestimate SM in part bare soil areas.

D. Estimation of Soil Moisture by Regression Algorithms

We can see in part C of the Results section, the best semiempirical models are needed to be selected reasonably according to land cover types and further effectively reflect the overall dryness and wetness distribution in the study area. Optical and SAR images have their respective advantages in estimating SM under different land cover types. Machine learning regression can take advantage of different data sources and establish their relationships with SM [103], [104].

Fig. 13 shows that in three traditional machine learning algorithms (GRNN, RFR, and SVR), the estimation accuracy of optical features (Group a or b) or SAR features (Group c) is significantly lower than that of combined optical and SAR features (Group d or e). On the whole, the estimation accuracy of Group (d) by RFR is the highest. *R* between estimated SM and measured SM is 0.9355. The MAE, MRE, and RMSE are 0.0224 cm^3/cm^3, 7.81%, and 0.0284 cm^3/cm^3, respectively. Estimation accuracy of Group (d) by GRNN is followed, with R of 0.9318, MAE, MRE, and RMSE of 0.0222 cm^3/cm^3, 0.0758, and 0.0288 cm^3/cm^3, respectively. The estimation accuracy of SVR is inferior to that of GRNN and RFR. When traditional spectral features (blue, green, red, NIR, nNIR, and corresponding vegetation indices), namely Group (a), are participated in the regression alone, the estimation accuracy of RFR is the highest, followed by GRNN. SVR is the worst. When all optical features are participated in the regression (Group b), the estimation accuracy of GRNN is the highest. RFR is followed and SVR is also worst. Compared with Group (a), the accuracy of Group (b) is greatly improved by GRNN (about 10%) and significantly reduced (about 15%) by SVR, respectively. The accuracy of RFR is slightly improved. This may be due to redundancy in the optical features. When SAR features (Group c) has participated in the regression alone, the estimation accuracy of RFR is the highest with RMSE of 0.0329 cm^3/cm^3, followed by GRNN (RMSE $=$ 0.0316 cm^3/cm^3) and SVR (RMSE $=$ 0.0398 cm^3/cm^3). The estimation accuracy of the three regression algorithms in Group (c) was slightly higher than that in Group (a). When traditional optical features and SAR features are involved in regression (Group d), the estimation accuracy is significantly improved. Estimation accuracy of RFR is the highest (RMSE $=$ 0.0284 cm^3/cm^3), followed by GRNN (RMSE $=$ 0.0288 cm^3/cm^3). SVR is also the worst, but the accuracy is fine (RMSE $=$ 0.0314 cm^3/cm^3). When all-optical and SAR features (Group e) were involved in regression, estimation accuracy by RFR is also the highest (RMSE $=$ 0.0299 cm^3/cm^3), but it is slightly lower than Group (d). Accuracy of SVR and GRNN is similar, but compared with Group (d), the accuracy dropped slightly.

Fig. 14(a) indicates that, with the increase of iterations, the estimation accuracy of DNN fluctuates sharply. After a certain number of iterations (about 75), the accuracy declines steadily. When the iteration reaches 13, as shown in Fig. 14(b), RMSE between estimated SM and measured SM is the smallest, only 0.0045 cm^3/cm^3. The corresponding R, MAE, and MRE are

0.9980, 0.0039 cm^3/cm^3, and 1.05%, respectively. However, with the increase of iteration times, the accuracy decreases obviously. When the number of iterations increases by two (about 15), RMSE is down to 0.1 cm^3/cm^3. When the number of iterations increases by five (about 18), RMSE is down to 0.2 cm^3/cm^3. Therefore, the number of iterations affects the final estimation results when the construction of DNN is completed. The above result indicates that the accuracy of SM by DNN is much higher than that of traditional machine learning.

V. Discussions

A. Optimal Filtering Method for Estimating SM by Sentinel-1

The radar backscattering coefficient is the direct reflection of surface SM and roughness, but it is easily affected by speckle noise and radar system parameters. Accurate estimation of the coefficients in the semiempirical models and accurate suppression of the influence of speckle noise is the key to accurately estimate SM in bare soil areas. This article discussed the filtering performance of seven filtering algorithms and their influences on SM estimation. We find that the Lee sigma filter can effectively suppress speck noise for different polarization backscattering coefficients under different land cover. In the last five years of research on estimating SM with 10–20 m resolutions by dual-polarized Sentinel-1 data, the filtering methods of SAR backscattering were different. Most studies employed Refined Lee filter [26], [105]–[110]. A small number of studies employed Mean filter [111], [112] and Lee filter [113], [114]. Some studies did not filter the backscattering coefficients images of Sentinel-1 [115], [116] or did not explain the filtering methods [117]–[120]. This article finds that the filtering effect of the Refined Lee filter for SM extraction is reasonable, but still inferior to the Lee sigma filter. If the VH backscattering coefficient after Mean or Lee filtering methods is used to estimate SM, the error in vegetation-covered areas is inestimable. For the above, the Lee sigma filter is the most suitable backscattering coefficient filtering method for estimating SM in the study area.

B. Comparison of Estimating SM Between SAR and Optics

For bare soil covered areas, optical remote sensing images can directly reflect the surface spectral information (SM and soil texture) after precise atmospheric correction. Many studies use SWIR bands to estimate SM with higher monitoring accuracy than other optical indices (such as NIR bands or land surface temperature) [74], [75]. As a strong absorptive band of water vapor, SWIR bands can effectively reflect SM in bare soil areas. Ma *et al.* (2018) used dual-polarized Sentinel-1 data to invert SM and compared it with the SMMI (soil moisture monitor index) based on Landsat images. The results showed that SMMI from NIR-SWIR2 space could effectively reflect the surface dryness and wetness conditions in the semi-arid area of China, which was consistent with the SAR results [121]. Tripathi *et al.* (2020) employed dual-polarized Sentinel-1 data to invert surface SM in farmland and used NDMI based on Sentinel-2 as the verification data. The results showed that estimated SM results by SAR and optics were highly correlated [122]. The above studies lack a comprehensive comparison between SAR estimation results and optical estimation results by SWIR bands under different vegetation cover conditions. In this article, MSMMI and MPDI from SWIR1-SWIR2 based on Sentinel-2 were used as optical models to estimate SM. We find that MSMMI can more precisely estimate SM in the bare soil areas, which was slightly better than the dual-polarization Sentinel-1 result, and better than MPDI. The optical models can effectively reflect the dryness and wetness condition of bare soil without the support of measured data. It can be seen from Fig. 6 that the combined (14) and (15) can realize the estimation of SM by VV and VH polarization, however, there are still a small number of sample points outside the 20% error bias line. These sample points underestimated [the black circle in Fig. 9(a)] were mainly located in the bare soil areas in the northwest of the study area with relatively low roughness (s was 0.53 cm, and l was 4.5 cm). The sample points overestimated [the red arrow in Fig. 9(a)] was located in the bare soil areas in the north of the study area with relatively high roughness (s was 1.13 cm, and l was 31.5 cm). Other studies have also shown that SM will be underestimated by SAR when roughness is low and overestimated when roughness is high [11], [12]–[14]. Surface roughness is one of the important factors that affect the accuracy of the estimated SM by SAR. For areas with very high or very low roughness, the SAR model monitoring effect still needs to be improved. When the surface roughness is high and the radar signal value is saturated, the estimated SM by SAR model in this study will have a large error. The SAR model has good estimation results in the range of $s < 1.5$ cm and $l \in (4,18)$ cm. When s is greater than 2 cm and l is greater than 18 cm, the error of the model is larger. To further improve the estimation accuracy of SM, in the future, full-polarization SAR data can be used to estimate SM.

For vegetation-covered areas, SM indices obtained by optical remote sensing often reflect crop canopy information, which can only indirectly estimate SM under the vegetation-covered areas. Vegetation types, VWC, growth stage, water retention ability, and the lag of SM response will affect the spectral information, and further influence the accuracy of SM estimation. Due to the penetration of radar remote sensing, it is more suitable for estimating SM in vegetation-covered areas, which is especially obvious in high FVC. The influence of vegetation on the microwave signal may be far greater than that of SM when FVC is high. Therefore, it is very important to correct the influence of vegetation, especially for the Sentinel-1 C-band. Optical remote sensing images can precisely simulate vegetation biochemical parameters through the characteristic changes of reflected radiation of ground objects. VWC is mainly used to represent vegetation information in the WCM model. We compared seven CWC indices and five biomass parameters obtained by the SNAP biomass module. The results showed that SRWI, LAI, and CWC (the latter two are derived from SNAP) have strong linear relationships with measured VWC. Estimated VWC from LAI has the lowest MAE and RMSE, so it is taken as the vegetation parameter in the WCM model. Many previous studies used LAI as input parameters of WCM [123], [124]. LAI can be acquired indirectly from other vegetation indices or physical models or measured data. At present, the common

LAI product is MOD15A2 data with low resolution [125]. The biophysical quantity module specially designed for Sentinel-2 data can more easily obtain the biomass indices such as LAI and CWC with 10–20 m spatial resolution that can represent VWC. For other remote sensing satellites such as Landsat and Gaofen, SRWI is an alternative index. In this article, the vegetation SM samples were mainly wheat and canola, with different growth and development stages, which included low to high FVC. After removing the influence of vegetation, VH polarization is slightly superior to VV polarization in estimating SM in medium and low vegetation cover areas ($0.30 \leq \text{FVC} < 0.60$), while it is lower than VV polarization in high vegetation cover areas ($\text{FVC} > 0.60$). That is mainly because copolarization has better penetrability and can better reflect the information on the underlying surface of closed vegetation. The cross-polarization signals contain the volume scattering of vegetation. Moreover, VV polarization is more suitable for monitoring the SM of wheat crops, while VH polarization is more suitable for canola. This is consistent with previous studies of Mercier *et al.* [126], El *et al.* [127], Xing *et al.* [128], and Kumar *et al.* [129]. El *et al.* (2019) showed that for C-band SAR when NDVI was between 0.4 and 0.7, the correlation between VH polarization and SM in vegetation-covered areas was slightly higher than that between VV polarization [127]. The disadvantage of using WCM and SAR to invert SM in vegetation-covered areas is that the WCM model ignores the second-order contribution of multiple scattering between soil and vegetation, it may not be suitable for estimating SM of tall crops [27], [124], [128]. Besides, LAI obtained by SNAP is underestimated compared with measured LAI data, which may further affect the estimation accuracy of SM. Therefore, future studies still need to explore the suitability of WCM introduced into LAI for monitoring SM of other crops.

Finally, SAR and optics were combined to estimate SM in the study area. Sentinel-2A data was used to estimate SM in the bare soil areas by the MSMMI index. The VV and VH polarization backscattering coefficients of Sentinel-1A data were used to estimate SM in the wheat and canola fields, respectively. We can find from Fig. 15 that R between estimated SM and measured SM can be increased to 0.8886. The corresponding MAE, MRE, and RMSE is 0.0301 cm^3/cm^3, 10.23%, and 0.0391 cm^3/cm^3, respectively. Most SM scatter points are within the 5% error lines. The above results indicate that the estimation accuracy of combined SAR data and optical data will be improved [26], [38], [107], [108], [113], [120], [122].

C. Comparison of Estimating SM by Regression Algorithms

Spectral features of optical images have different responses to SM in bare soil or vegetation-covered areas. Soil structure, soil surface roughness, organic matter content, and vegetation types will affect the accuracy of estimating SM. For SAR data, the permittivity of soil increases in an approximately linear way with the increase of SM, resulting in a decrease in emissivity. This linear relationship is not immutable and is affected by SAR frequency, incident angle, and surface roughness. With the increase of roughness, emissivity decreases slowly with SM.

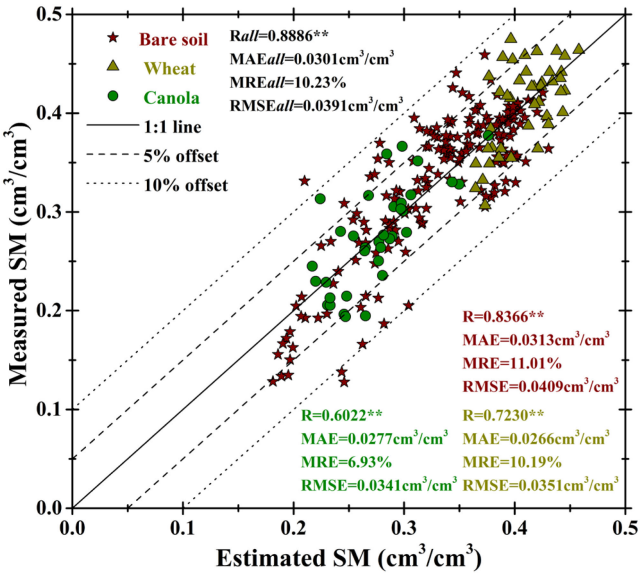

Fig. 15. Estimated SM under different land cover types by combining Sentinel-1A and Sentinel-2A.

However, response degrees of different land cover to SM are difficult to be expressed by conventional statistical methods. Powerful nonlinear fitting characteristics of machine learning can precisely describe relationships between remote sensing data and SM.

Among three traditional machine learning algorithms, the combination of the traditional optical spectrum (blue, green, red, NIR, and corresponding vegetation indexes) and SAR (VV, VH polarization, and radar incident angle) can effectively estimate SM. But too many optics features may slightly increase or even decrease final accuracies by traditional machine learning regression. RFR has an excellent regression performance, which is equal to GRNN and better than SVR.

RF is a classifier containing multiple decision trees. The mode of output category is used to improve the accuracy of prediction and control overfitting. In the five regression experiments, the estimation accuracy of Group (d) (namely SAR features and traditional optical features) by RFR is the highest. RMSE between estimated SM and measured SM is 0.0284 cm^3/cm^3. Compared with the estimation results of combining SAR and optical semiempirical models (Fig. 15), the accuracy of the RFR regression model is improved by about 27.37% (Relative to RMSE). The excellent regression ability of RFR on estimating SM had also been confirmed in many studies [130], [131].

GRNN is also widely used in SM estimation and prediction, but few studies are comparing its performance with RFR [133]. We find that GRNN has a good regression performance, for example, in Group (b) (namely all optical features participation), estimation accuracy by GRNN is the highest (RMSE = 0.0308 cm^3/cm^3) which slightly higher than RFR. In other regression experiments, GRNN was slightly weaker than RFR. Also, the accuracies of all regression models by GRNN and RFR are better than those of semi-empirical SM models.

SVR has a worst regression performance in the five regression experiments, for example, when only optical features are

TABLE III
FEATURES USED FOR SOIL MOISTURE ESTIMATION BY RFR

Groups (number)	Description
a1 (11)	Traditional spectrum
b1 (33)	Tradition + Red edge
c1 (17)	Tradition + SWIR
d1 (39)	Tradition + Red edge + SWIR
e1 (44)	Tradition + Red edge + SWIR + Biomass
f1 (16)	Traditional spectrum + SAR
g1 (15)	f1 (***no incident angle***)
h1 (38)	Tradition + Red edge + SAR
i1 (22)	Tradition + SWIR + SAR
j1 (44)	Tradition + Red edge + SWIR + SAR
k1 (49)	Tradition + Red edge + SWIR + Biomass + SAR
l1 (48)	k1 (***no incident angle***)
m1 (5)	SAR
n1 (4)	SAR (***no incident angle***)

Note: The groups in italic bold are the same as those in Table II.

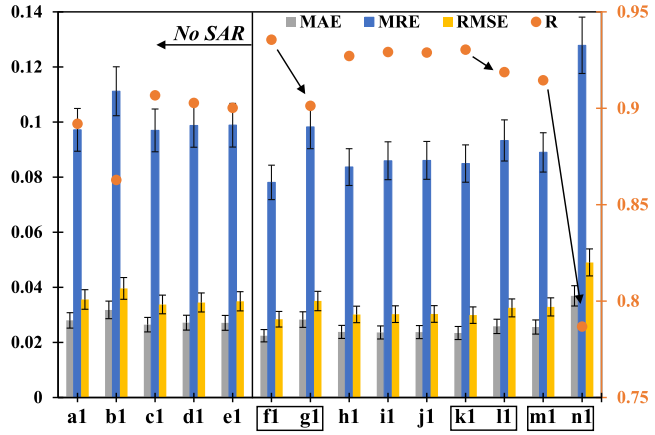

Fig. 16. Accuracy of estimated SM based on RFR for different characteristic variable groups.

included (Group a or b) are included, the estimation accuracy of SVR will be greatly reduced and lower than that of semiempirical SM models. This conclusion contradicts previous research [109], [134]. This indicates that there may are many redundant features in the optical features. The robustness of SVR is inadequate when dealing with redundant feature sets. However, the estimation accuracy of SM combining optical data and SAR data by SVR is reasonable, although lower than RFR or GRNN.

The above results indicate that the RFR algorithm has relatively high estimation accuracy and also can evaluate the importance of input variables to the predicted results [41], [85], [130], [131]. We further subdivided and added the feature variable groups (Table III) to explore the influence of traditional spectrum features, red edge spectrum features, SWIR spectrum features, biomass features, and SAR features on the estimation of SM by RFR. Among them, Group (a)–(e) in Table II is consistent with Group (a1), (e1), (f1), (k1), and (m1) in Table III. Group (b1) contains both traditional and red edge spectrum features. Group (c1) contains both traditional and SWIR spectrum features. Group (d1) contains traditional, red edge, and SWIR spectrum features. Group (g1) contains both traditional and SAR features without radar incident angle. Group (h1) contains traditional, red edge spectrum and SAR features. Group (i1) contains traditional, SWIR spectrum and SAR features. Group (j1) contains traditional, red edge, SWIR spectrum, and SAR features. Group (l1) contains traditional, red edge spectrum, biomass, and SAR features without radar incident angle. Group (n1) contains SAR features but no radar incidence angle.

Fig. 16 shows that on the whole, the estimation accuracy of the combined optics and SAR images is higher than that of the optical or SAR images alone. When the SAR feature was used alone (Group m1) to estimate SM, good accuracy can be achieved, with R of 0.9145 and RMSE of 0.0329 cm^3/cm^3. When the radar incidence angle did not participate in regression (Group n1), the accuracy decreased obviously (about 48.94%, relative to the RMSE), with R of 0.7867 and RMSE of 0.049 cm^3/cm^3. When traditional spectrum and SAR features (Group f1) participated in regression, the estimation accuracy is also the highest, with R of 0.9355 and RMSE of 0.0284 cm^3/cm^3. However, RMSE accuracy decreased by about 23.33% without incident angle participation (Group g1). Groups k1 and l1 had similar results. This indicates that the radar incidence angle can effectively improve the accuracy of SM estimation by SAR features. When only traditional spectrum features were involved in regression (Group a1), the estimation accuracy was relatively low, R and RMSE were 0.8919 and 0.0356 cm^3/cm^3, respectively. The introduction of all red edge spectrum feature (Group b1) will reduce the RMSE accuracy by about 11.23%. The introduction of SWIR or biomass features (Group c1 and d1) will improve the estimation accuracy, but the improvement is low and less than that of the introduction of SAR. When traditional spectrum, red edge, SWIR, biomass, and SAR features were involved in regression (Group h1, i1, j1, and k1), the accuracy was basically the same, obviously higher than that of optical or SAR features alone, but slightly lower than that of the traditional spectrum and SAR features (Group f1). This indicates that combined optical and SAR features can effectively improve the accuracy of SM estimation. When SAR features are involved in regression, the estimation accuracy of introducing features such as red edge, SWIR, or biomass is lower than that of traditional spectrum features. Radar incidence angle has great influences on estimating SM by SAR features, so it needs to be considered in practical application.

In addition, we ranked the importance scores (by RFR) of each variable with measured SM and explored the relationship between the number of features and the accuracy of estimated SM. Fig. 17 shows that the top 10 variables of importance to measured SM are SWIR1, Red edge1, SWIR2, VH, VV-VH, NDVIre3, VV, green, MRESR, and EVI. All SAR features scored high in importance. In optical features, the importance scores of reflectance bands were higher than those of multiband vegetation indices. The top scores of traditional spectrum features are green, EVI, NIR, and red, while DVI, RVI, NDVI, and MSAVI scored relatively low. The top scores of red edge features are red edge1, NDVIre3, MRESR, ARI1, MTCI, and S2REP. This is mainly because these indices contain the Red edge1 band (705 nm) of Sentinel-2, which is conducive to reflecting the growth and development status of vegetation, thus effectively representing

TABLE IV
ADVANTAGES AND DISADVANTAGES OF DIFFERENT SOIL MOISTURE ESTIMATION METHODS

Methods and data	Advantages	Disadvantages
Semi-empirical SAR model: Sentinel-1A	1. High estimation accuracy in vegetation-covered areas. 2. Stable imaging at equal intervals.	1. Measured surface roughness data needed. 2. Measured VWC data needed in vegetation-covered areas.
Optical model: Sentinel-2A	1. High estimation accuracy in bare soil areas. 2. SM can be monitored without measured data.	1. SM underestimated in vegetation areas. 2. Stable imaging can not meet during the phenological stage of crops.
Traditional machine learning regression models: (GRNN/RFR/SVR) Sentinel-1A/2A	1. Higher estimation accuracy. 2. High efficiency and simple parameters.	1. Measured SM data required for modeling. 2. Input features need to be selected.
Deep learning regression model: (DNN) Sentinel-1A/2A	Perfect estimation accuracy.	1.Measured SM data required for modeling. 2. Lots of time needed to set up a network.

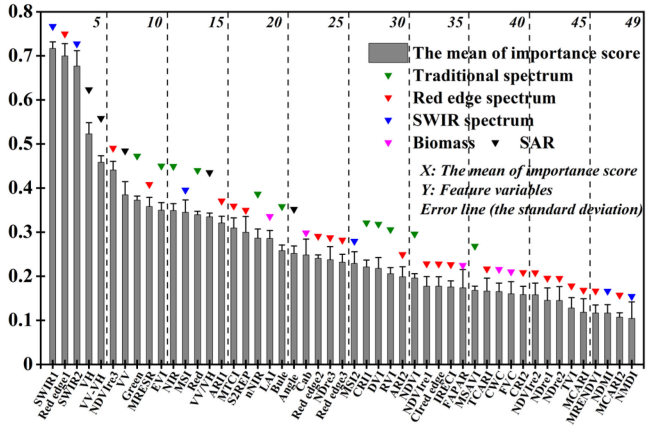

Fig. 17. Distribution of importance score of each variable to measured SM.

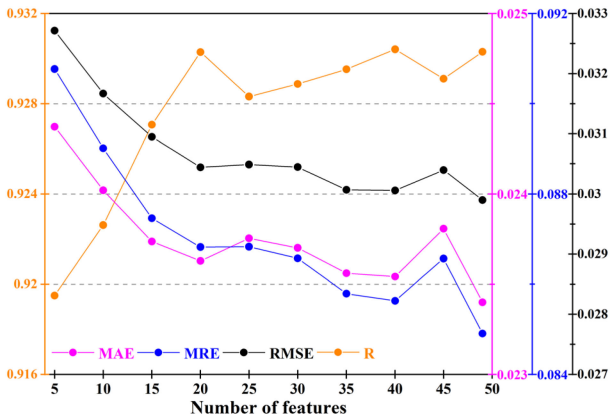

Fig. 18. Relationship between the number of optimizing features and the accuracy of estimated SM based on RFR.

the SM on the underlying surface [135]. The remaining red edge features had little effect on the estimation of SM due to low importance. The top scores of SWIR features are SWIR1, SWIR2, and MSI, while NDMI and NMDI scored low. This is mainly because SWIR are water-absorbing bands, both for bare soil areas and vegetation-covered areas, and they can reflect the surface SM. The above analysis also indicates that SAR and optical features have respective advantages in estimating SM.

According to the ranking of feature importance (Fig. 17), the estimation accuracy of each feature group was obtained by accumulating five features. Fig. 18 shows that the estimation accuracy of RFR shows a sharp increase with the increase in the number of features (the first 20), followed by a slow rise in fluctuation. When the number of features reached 20, 40, and 49, respectively, the R between estimated SM and measured SM reached the maximum value (about 0.9302), and the estimation accuracy had been improved steadily, RMSE reaching 0.0299 cm^3/cm^3 with 49 features. The estimation accuracy (RMSE) of 20 features was about 6.95% higher than that of five features, while the estimation accuracy of 40 and 49 features was only 1.26% and 1.78% higher than that of 20 features, respectively. This indicates that the estimation accuracy increased with the increase in the number of optimizing features, but the improvement was low after the number of features reached 20. Besides, the estimation accuracy of the optimizing features is still lower than that of the traditional spectrum and SAR features (Group f1 in Table III).

In DNN, the optimization extremum solution of the loss function is generally completed step by step by iteration through the gradient descent method. The number of iterations has a great influence on the final prediction result of DNN. Too many iterations will significantly reduce the prediction accuracy. In this article, when the number of iterations reaches 13 after the framework of DNN is built, RMSE between estimated SM and measured SM was only 0.0045 cm^3/cm^3. DL's powerful nonlinear fitting ability can be adaptive to input feature variables through multilayer networks. Achieng *et al.* (2019) also came to a similar conclusion that the estimation accuracy of SM by DNN was significantly better than that of ANN. The estimation accuracy by DNN in the test set could reach 0.003 cm^3/cm^3 [134]. This indicates that DL regression based on SAR and optical remote sensing data can estimate SM in farmland with great accuracy, which is better than the traditional machine learning algorithms [134], [136].

Although DL can almost perfectly fit relationships between different remote sensing data and measured SM, it needs to spend a lot of time building the network framework and adjust the optimal parameters. The accuracy and operability of RFR and GRNN make them powerful tools for estimating SM using SAR and optical data. Table IV shows the advantages

and disadvantages of SM estimation methods used in this article. Nowadays, optical remote sensing satellites are developing in the direction of hyper-spectrum, high temporal resolution, and high spatial resolution. Radar remote sensing satellites are developing towards multipolarization, multi-incidence angle, and multimode. There are also more and more ground stations that can measure various surface parameters. Remote sensing satellites and measured stations play different roles and tasks. Machine learning algorithms can effectively excavate the close relationships between abundant satellite remote sensing data and land surface parameters [137]–[139]. Combined optical and SAR satellite data through machine learning regression has great potential in precisely monitoring SM in farmland, which can provide decision bases and strong guarantees for agricultural crop production and development status.

VI. Conclusion

The influence of different filtering algorithms for the backscattering coefficients on estimating SM was compared in this article. We find that the dual-polarized Sentinel-1A backscattering (VV and VH) after the Lee sigma filter have the highest correlation with the measured SM under different land cover types. Therefore, the Lee sigma filter can be used as the best filtering method for backscattering coefficients to estimate SM at the pixel scale. Dual-polarized backscattering coefficients and combined roughness ($Rs = s^3/l^2$) were used to jointly estimate SM in bare soil areas (FVC $\leq$ 0.30). The estimation accuracy was slightly lower than the results obtained by the optical index (MSMMI from the SWIR1–SWIR2 feature space of Sentinel-2A). After removing influences of vegetation cover on the backscattering by using WCM introduced into LAI, the estimated accuracy of SM by VH polarization is higher than that by VV polarization. But in high vegetation cover areas (FVC $>$ 0.60), the conclusion is the opposite. The estimation accuracy of SM in vegetation-covered areas by Sentinel-1A is higher than that of Sentinel-2A. On the whole, optical and SAR images have their respective advantages in estimating SM under different cover types. Optical remote sensing has slightly higher accuracy in estimating SM in bare soil areas, while SAR has conspicuously higher accuracy in vegetation cover areas. The estimation accuracy of SM by combining Sentinel-1 with Sentinel-2 is significantly better than that by the optical data alone. The RMSE between the estimated SM and the measured SM is 0.0391 cm^3/cm^3. Finally, four machine learning regression algorithms were used to estimate SM in the study area. The results show that the estimation accuracies by regression algorithms were much higher than those of the semiempirical SAR and optical models. Among traditional machine learning algorithms, the estimation accuracy of RFR and GRNN is the same, which is better than SVR. The accuracy in estimating SM by RFR combining SAR and traditional spectral information (blue, green, red, NIR, and corresponding vegetation indices) is the highest, with an RMSE of 0.0284 cm^3/cm^3. The estimation accuracy of SM by SAR and optical data by DNN is up to 0.0045 cm^3/cm^3. There are great potentials to combine Sentinel-1 with Sentinel-2 data to precisely estimate SM in farmland by machine learning regression algorithms.

Acknowledgment

The authors would like to sincerely thank Copernicus Open Access Hub for providing Sentinel-1A and Sentinel-2A images, and NASA's Earth Observing System Data and Information System for providing the SMAPVEX16 field dataset. They were also very grateful to every scientist who has contributed to the SMAPVEX16 dataset. They were very grateful to the two anonymous reviewers whose comments have been of great help in the revision of the study.

References

[1] Y. Liu, Y. Liu, and W. Wang, "Inter-comparison of satellite-retrieved and global land data assimilation system-simulated soil moisture datasets for global drought analysis," *Remote Sens. Environ.*, vol. 220, pp. 1–18, 2019.
[2] J. C. Price, "Thermal inertia mapping: A new view of the earth," *J. Geophys. Res.*, vol. 82, no. 18, pp. 2582–2590, 1977.
[3] J. C. Price, "On the analysis of thermal infrared imagery: The limited utility of apparent thermal inertia," *Remote Sens. Environ.*, vol. 18, no. 1, pp. 59–73, 1985.
[4] I. Sandholt, K. Rasmussen, and J. Andersen, "A simple interpretation of the surface temperature/vegetation index space for assessment of surface moisture status," *Remote Sens. Environ.*, vol. 79, no. 2–3, pp. 213–224, 2002.
[5] R. B. Myneni, S. O. Los, and C. J. Tucker, "Satellite-based identification of linked vegetation index and sea surface temperature anomaly areas from 1982–1990 for Africa, Australia and South America," *Geophys. Res. Lett.*, vol. 23, no. 7, pp. 729–732, 2013.
[6] S. M. Quiring and S. Ganesh, "Evaluating the utility of the vegetation condition index (VCI) for monitoring meteorological drought in texas," *Agricultural Forest Meteorol.*, vol. 150, no. 3, pp. 330–339, 2010.
[7] P. Wang, J. Gong, and X. Li, "Vegetation-temperature condition index and its application for drought monitoring," in *Proc. IEEE Int. Geosci. Remote Sens. Symp.*, 2001, pp. 141–143.
[8] A. Ghulam, T. M. Kusky, T. Teyip, and Q. Qin, "Sub-canopy soil moisture modeling in n-dimensional spectral feature space," *Photogramm. Eng. Remote Sens.*, vol. 77, no. 2, pp. 149–156, 2011.
[9] J. Pan and T. Li, "Extracting desertification from landsat TM imagery based on spectral mixture analysis and albedo-vegetation feature space," *Natural Hazards*, vol. 68, no. 2, pp. 915–927, 2013.
[10] C. Wu, Q. Qin, M. Li, and N. Zhang, "Soil moisture monitoring of vegetative area in farmland by remote sensing based on spectral feature space," *Trans. Chin. Soc. Agricultural Eng.*, vol. 30, no. 16, pp. 106–112, 2014.
[11] Y. Oh, K. Sarabandi, and F. T. Ulaby, "An empirical model and an inversion technique for radar scattering from bare soil surfaces," *IEEE Trans. Geosci. Remote Sens.*, vol. 30, no. 2, pp. 370–381, Mar. 1992.
[12] T. Neusch and M. Sties, "Application of the Dubois-model using experimental synthetic aperture radar data for the determination of soil moisture and surface roughness," *ISPRS-J. Photogramm. Remote Sens.*, vol. 54, no. 4, pp. 273–278, 1999.
[13] J. Shi, J. Wang, A. Y. Hsu, P. E. O'Neill, and E. T. Engman, "Estimation of bare surface soil moisture and surface roughness parameter using L-band SAR image data," *IEEE Trans. Geosci. Remote Sens.*, vol. 35, no. 5, pp. 1254–1266, Sep. 1997.
[14] B. Nicolas *et al.*, "A new empirical model for radar scattering from bare soil surfaces," *Remote Sens.*, vol. 8, no. 11, 2016, Art. no. 920.
[15] T. D. Wu, K. S. Chen, J. Shi, H. W. Lee, and A. K. Fung, "A study of an AIEM model for bistatic scattering from randomly rough surfaces," *IEEE Trans. Geosci. Remote Sens.*, vol. 46, no. 9, pp. 2584–2598, Sep. 2008.
[16] D. Klement and J. Preissner, "Special problems in applying the physical optics method for backscatter computations of complicated objects," *IEEE Trans. Antennas Propag.*, vol. 36, no. 2, pp. 228–237, Feb. 1988.
[17] M. Chen and A. Fung, "A numerical study of the regions of validity of the kirchhoff and small-perturbation rough surface scattering models," *Radio Sci.*, vol. 23, no. 2, pp. 163–170, 1988.
[18] M. E. Hajj, N. Baghdadi, and M. Zribi, "Comparative analysis of the accuracy of surface soil moisture estimation from the C- and L-bands," *Int. J. Appl. Earth Observ. Geoinf.*, vol. 82, 2019, Art. no. 101888.
[19] F. D. F. F. Schiavon, "Retrieving soil moisture and agricultural variables by microwave radiometry using neural networks," *Remote Sens. Environ.*, vol. 84, no. 2, pp. 174–183, 2003.

[20] D. Nagesh Kumar, K. S. Raju, and B. Ashok, "Optimal reservoir operation for irrigation of multiple crops using genetic algorithms," *J. Irrigation Drainage Eng.-ASCE*, vol. 132, no. 2, pp. 123–129, 2006.

[21] N. Baghdadi, R. Cresson, M. El Hajj, R. Ludwig, and I. La Jeunesse, "Soil parameters estimation over bare agriculture areas from C-band polarimetric SAR data using neural networks," *Hydrol. Earth System Sci. Discuss.*, vol. 9, no. 3, pp. 2897–2933, 2012.

[22] F. T. Ulaby, K. Sarabandi, K. Mcdonald, M. Whitt, and M. C. Dobson, "Michigan microwave canopy scattering model," *Int. J. Remote Sens.*, vol. 11, no. 7, pp. 1223–1253, 1990.

[23] M. A. Karam, A. K. Fung, R. H. Lang, and N. S. Chauhan, "A microwave scattering model for layered vegetation," *IEEE Trans. Geosci. Remote Sens.*, vol. 30, no. 4, pp. 767–784, Jul. 1992.

[24] R. D. De Roo, Y. Du, F. T. Ulaby, and M. C. Dobson, "A semi-empirical backscattering model at L-band and C-band for a soybean canopy with soil moisture inversion," *IEEE Trans. Geosci. Remote Sens.*, vol. 39, no. 4, pp. 864–872, Apr. 2001.

[25] E. P. W. Attema and F. T. Ulaby, "Vegetation modeled as a water cloud," *Radio Sci.*, vol. 13, no. 2, pp. 357–364, 1978.

[26] E. H. Mohammad, B. Nicolas, Z. Mehrez, and B. Hassan, "Synergic use of Sentinel-1 and Sentinel-2 images for operational soil moisture mapping at high spatial resolution over agricultural areas," *Remote Sens.*, vol. 9, no. 12, 2017, Art. no. 1292.

[27] N. Baghdadi, H. M. El, M. Zribi, and S. Bousbih, "Calibration of the water cloud model at C-Band for winter crop fields and grasslands," *Remote Sens.*, vol. 9, no. 9, 2018, Art. no. 969.

[28] M. Piles, D. Entekhabi, and A. Camps, "A change detection algorithm for retrieving high-resolution soil moisture from SMAP radar and radiometer observations," *IEEE Trans. Geosci. Remote Sens.*, vol. 47, no. 12, pp. 4125–4131, Dec. 2009.

[29] B. J. Cosby, G. M. Hornberger, R. B. Clapp, and T. R. Ginn, "A statistical exploration of the relationships of soil moisture characteristics to the physical properties of soils," *Water Resour. Res.*, vol. 20, no. 6, pp. 682–690, 1984.

[30] T. Pellarin, J. C. Calvet, and J. P. Wigneron, "Surface soil moisture retrieval from L-band radiometry: A global regression study," *IEEE Trans. Geosci. Remote Sens.*, vol. 41, no. 9, pp. 2037–2051, Sep. 2003.

[31] N. Baghdadi, N. Holah, and M. Zribi, "Soil moisture estimation using multi-incidence and multi-polarization ASAR data," *Int. J. Remote Sens.*, vol. 27, no. 9/10, pp. 1907–1920, 2006.

[32] M. Zribi and M. Dechambre, "A new empirical model to retrieve soil moisture and roughness from C-band radar data," *Remote Sens. Environ.*, vol. 84, no. 1, pp. 42–52, 2002.

[33] J. Chen, Y. Jia, and F. Yu, "Estimation of bare surface soil moisture by dual polarization radar," *J. Agricultural Eng. (Chin. J.)*, vol. 29, no. 10, pp. 109–115, 2013.

[34] A. Ghulam, Q. Qin, T. Teyip, and Z. L. Li, "Modified perpendicular drought index (MPDI): A real-time drought monitoring method," *ISPRS-J. Photogramm. Remote Sens.*, vol. 62, no. 2, pp. 150–164, 2007.

[35] Y. Liu, Y. Li, Y. Lu, and H. Yue, "Comparison and application of MPDI and MSMMI for drought monitoring in desert mining area," in *Proc. Conf. Ser., Earth Environ. Sci.*, vol. 146, Art. no. 012001.

[36] L. Liu, J. Wang, Y. Bao, W. Huang, Z. Ma, and C. Zhao, "Predicting winter wheat condition, grain yield and protein content using multi-temporal EnviSat-ASAR and Landsat TM satellite images," *Int. J. Remote Sens.*, vol. 27, no. 4, pp. 737–753, 2006.

[37] I. Gherboudj, R. Magagi, A. A. Berg, and B. Toth, "Soil moisture retrieval over agricultural fields from multi-polarized and multi-angular RADARSAT-2 SAR data," *Remote Sens. Environ.*, vol. 115, no. 1, pp. 33–43, 2011.

[38] G. Qi, Z. Mehrez, E. Maria, and B. Nicolas, "Synergetic use of Sentinel-1 and Sentinel-2 data for soil moisture mapping at 100 m resolution," *Sensors*, vol. 17, no. 9, 2017, Art. no. 1966.

[39] H. Z. Li, S. Guo, C. J. Li, and J. Q. Sun, "A hybrid annual power load forecasting model based on generalized regression neural network with fruit fly optimization algorithm," *Knowl. Syst.*, vol. 37, pp. 378–387, 2013.

[40] B. Schölkopf, P. Bartlett, A. Smola, and R. Williamson, "Shrinking the tube: A new support vector regression algorithm," in *Proc. Conf. Adv. Neural Inf. Process. Syst. II*, 1999, pp. 330–336.

[41] A. Liaw and M. Wiener, "Classification and regression by randomForest," *R News*, vol. 2, no. 3, pp. 18–22, 2002.

[42] W. Liu, Z. Wang, X. Liu, N. Zeng, Y. Liu, and F. E. Alsaadi, "A survey of deep neural network architectures and their applications," *Neurocomputing*, vol. 234, pp. 11–26, 2017.

[43] H. McNairn, K. Gottfried, and J. Powers, "SMAPVEX16 manitoba meteorological data. Version 1," in *Proc. NASA Nat. Snow Ice Data Center Distrib. Act. Arch. Center*, 2018.

[44] H. McNairn, K. Gottfried, and J. Powers, "SMAPVEX16 manitoba land cover classification map. Version 1," in *Proc. NASA Nat. Snow Ice Data Center Distrib. Act. Arch. Center*, 2018.

[45] H. McNairn, K. Gottfried, and J. Powers, "SMAPVEX16 manitoba in situ vegetation data. Version 1," in *Proc. NASA Nat. Snow Ice Data Center Distrib. Act. Arch. Center*, 2018.

[46] H. McNairn, K. Gottfried, and J. Powers, "SMAPVEX16 manitoba leaf area index. Version 1," in *Proc. NASA Nat. Snow Ice Data Center Distrib. Act. Arch. Center*, 2018.

[47] H. McNairn, K. Gottfried, and J. Powers, "SMAPVEX16 manitoba surface roughness data. Version 1," in *Proc. NASA Nat. Snow Ice Data Center Distrib. Act. Arch. Center*, 2018.

[48] H. McNairn, K. Gottfried, and J. Powers, "SMAPVEX16 manitoba probe-based in situ soil moisture data. Version 1," in *Proc. NASA Nat. Snow Ice Data Center Distrib. Act. Arch. Center*, 2018.

[49] D. Entekhabi *et al.*, "The soil moisture active passive (SMAP) mission," *Proc. IEEE*, vol. 98, no. 5, pp. 704–716, May 2010.

[50] Q. Hu, J. Yang, B. Xu, J. Huang, and K. Liu, "Evaluation of global decametric-resolution LAI, FAPAR and FVC estimates derived from Sentinel-2 imagery," *Remote Sens.*, vol. 12, no. 6, 2020, Art. no. 912.

[51] C. López-Martínez and X. Fàbregas, "Polarimetric SAR speckle noise model," *IEEE Trans. Geosci. Remote Sens.*, vol. 41, no. 10, pp. 2232–2242, Oct. 2003.

[52] J. S. Lee, "Digital image smoothing and the sigma filter," *Comput. Vis. Graph. Image Process.*, vol. 24, no. 2, pp. 255–269, 1983.

[53] D. T. Kuan, A. A. Sawchuk, T. C. Strand, and P. Chavel, "Adaptive noise smoothing filter for images with signal-dependent noise," *IEEE Trans. Pattern Anal. Mach. Intell.*, vol. PMAI-7, no. 2, pp. 165–177, Mar. 1985.

[54] A. Lopes, E. Nezry, R. Touzi, and H. Laur, "Structure detection and statistical adaptive speckle filtering in SAR images," *Int. J. Remote Sens.*, vol. 14, no. 9, pp. 1735–1758, 1993.

[55] Z. Shi and K. B. Fung, "A comparison of digital speckle filters," in *Proc Int. Geosci. Remote Sens. Symp.*, vol. 4, 1994, pp. 2129–2133.

[56] J. S. Lee, S. R. Cloude, K. P. Papathanassiou, M. R. Grunes, and I. H. Woodhouse, "Speckle filtering and coherence estimation of polarimetric SAR interferometry data for forest applications," *IEEE Trans. Geosci. Remote Sens.*, vol. 41, no. 10, pp. 2254–2263, Oct. 2003.

[57] F. Qiu, J. Berglund, J. Jensen, P. Thakkar, and D. Ren, "Speckle noise reduction in SAR imagery using a local adaptive median filter," *GIsci. Remote Sens.*, vol. 41, no. 3, pp. 244–266, 2004.

[58] J. S. Lee, J. S. Lee, J. H. Wen, T. L. Ainsworth, K. S. Chen, and A. J. Chen, "Improved sigma filter for speckle filtering of SAR imagery," *IEEE Trans. Geosci. Remote Sens.*, vol. 47, no. 1, pp. 202–213, Jan. 2009.

[59] J. S. Lee, "Refined filtering of image noise using local statistics," *Comput. Graph. Image Process.*, vol. 15, no. 4, pp. 380–389, 1981.

[60] M. Autret, R. Bernard, and D. Vidal-Madjar, "Theoretical study of the sensitivity of the microwave backscattering coefficient to the soil surface parameters," *Int. J. Remote Sens.*, vol. 10, no. 1, pp. 171–179, 1989.

[61] J. Shi, L. Jiang, L. Zhang, K. S. Chen, and W. J. Pierre, "A parameterized multifrequency-polarization surface emission model," *IEEE Trans. Geosci. Remote Sens.*, vol. 43, no. 12, pp. 2831–2841, Dec. 2005.

[62] M. Brogioni, S. Pettinato, G. Macelloni, S. Paloscia, and P. Pampaloni, "Sensitivity of bistatic scattering to soil moisture and surface roughness of bare soils," *Int. J. Remote Sens.*, vol. 31, no. 15, pp. 4227–4255, 2010.

[63] P. C. Dubois, J. Van Zyl, and T. Engman, "Measuring soil moisture with imaging radars," *IEEE Trans. Geosci. Remote Sens.*, vol. 33, no. 4, pp. 915–926, Jul. 2002.

[64] N. Baghdadi, N. Holah, and M. Zribi, "Calibration of the integral equation model for SAR data in C-band and HH and VV polarizations," *Int. J. Remote Sens.*, vol. 27, no. 4, pp. 805–816, 2006.

[65] N. Baghdadi, J. A. Chaaya, and M. Zribi, "Semiempirical calibration of the integral equation model for SAR data in C-Band and cross polarization using radar images and field measurements," *IEEE Geosci. Remote Sens. Lett.*, vol. 8, no. 1, pp. 14–18, Jan. 2011.

[66] N. Baghdadi, E. Saba, M. Aubert, M. Zribi, and F. Baup, "Comparison between backscattered TerraSAR signals and simulations from the radar backscattering models IEM, Oh, and Dubois," *IEEE Geosci. Remote Sens. Lett.*, vol. 6, no. 8, pp. 1160–1164, Jan. 2011.

[67] N. Baghdadi, C. King, A. Bourguignon, and A. Remond, "Potential of ERS and Radarsat data for surface roughness monitoring over bare agricultural fields: Application to catchments in northern France," *Int. J. Remote Sens.*, vol. 23, no. 17, pp. 3427–3442, 2002.

[68] J. R. G. Townshed and C. O. Justice, "Analysis of the dynamics of African vegetation using the normalized difference vegetation index," *Int. J. Remote Sens.*, vol. 7, no. 11, pp. 1435–1445, 1986.

[69] L. Brown, J. M. Chen, and S. G. Leblanc, "A shortwave infrared modification to the simple ratio for LAI retrieval in boreal forests: An image and model analysis," *Remote Sens. Environ.*, vol. 71, no. 1, pp. 16–25, 2000.

[70] P. Ceccato, S. Flasse, S. Tarantola, S. Jacquemoud, and J.-M. Grégoire, "Detecting vegetation leaf water content using reflectance in the optical domain," *Remote Sens. Environ.*, vol. 77, no. 1, pp. 22–33, 2001.

[71] S. Jin and S. A. Sader, "Comparison of time series tasseled cap wetness and the normalized difference moisture index in detecting forest disturbances," *Remote Sens. Environ.*, vol. 94, no. 3, pp. 364–372, 2005.

[72] L. Wang and J. J. Qu, "NMDI: A normalized multi-band drought index for monitoring soil and vegetation moisture with satellite remote sensing," *Geophys. Res. Lett.*, vol. 34, no. 20, 2007, Art. no. L20405.

[73] T. Schut, D. Stephens, R. Stovold, M. Adams, and R. Craig, "Improved wheat yield and production forecasting with a moisture stress index, AVHRR and MODIS data," *Crop Pasture Sci.*, vol. 60, no. 1, pp. 60–70, 2009.

[74] A. Ghulam, Z. L. Li, Q. M. Qin, Q. X. Tong, and J. H. Wang, "A method for canopy water content estimation for highly vegetated surfaces-shortwave infrared perpendicular water stress index," *Sci. China Ser. D: Earth Sci.*, vol. 50, no. 9, pp. 1359–1368, 2007.

[75] S. Koley and J. Chockalingam, "Estimation and evaluation of high spatial resolution surface soil moisture using multi-sensor multi-resolution approach," *Geoderma*, vol. 378, 2020, Art. no. 114618.

[76] D. Lu, "The potential and challenge of remote sensing-based biomass estimation," *Int. J. Remote Sens.*, vol. 27, no. 7/8, pp. 1297–1328, 2006.

[77] E. M. I. Adam and O. Mutanga, "Estimation of high density wetland biomass: Combining regression model with vegetation index developed from Worldview-2 imagery," in *Proc. Remote Sens. Agriculture Ecosyst. Hydrol.*, 2012, Art. no. 85310V.

[78] S. Chen, E. S. Chng, and K. Alkadhimi, "Orthogonal least squares learning algorithm for radial basis function networks," *IEEE Trans. Neural Netw.*, vol. 64, no. 5, pp. 829–837, Mar. 1991.

[79] M. K. Gill, T. Asefa, M. W. Kemblowski, and M. Mckee, "Soil moisture prediction using support vector machines1," *J. Amer. Water Resour. Assoc.*, vol. 42, no. 4, pp. 1033–1046, 2006.

[80] S. S. Durbha, R. L. King, and N. H. Younan, "Support vector machines regression for retrieval of leaf area index from multiangle imaging spectroradiometer," *Remote Sens. Environ.*, vol. 107, no. 1–2, pp. 348–361, 2007.

[81] D. Tuia, J. Verrelst, L. Alonso, F. Perez Cruz, and G. Camps Valls, "Multioutput support vector regression for remote sensing biophysical parameter estimation," *IEEE Geosci. Remote Sens. Lett.*, vol. 8, no. 4, pp. 804–808, Jul. 2011.

[82] Y. Everingham, J. Sexton, D. Skocaj, and G. Inman-Bamber, "Accurate prediction of sugarcane yield using a random forest algorithm," *Agron. Sustain. Develop.*, vol. 36, no. 2, 2016, Art. no. 27.

[83] L. A. Wang, X. Zhou, X. Zhu, Z. Dong, and W. Guo, "Estimation of biomass in wheat using random forest regression algorithm and remote sensing data," *Crop J.*, vol. 4, no. 3, pp. 212–219, 2016.

[84] Y. Huanhuan, Y. Guijun, L. Changchun, W. Yanjie, L. Jiangang, and Y. Haiyang, "Retrieving soybean leaf area index from unmanned aerial vehicle hyperspectral remote sensing: Analysis of RF, ANN, and SVM regression models," *Remote Sens.*, vol. 9, no. 4, 2017, Art. no. 309.

[85] Z. Wei, S. Nilda, L. Hui, and L. Ainong, "A spatial downscaling approach for the SMAP passive surface soil moisture product using random forest regression," *J. Hydrol.*, vol. 563, pp. 1009–1024, 2018.

[86] P. J. Werbos, "Backpropagation through time: What it does and how to do it," *Proc. IEEE*, vol. 78, no. 10, pp. 1550–1560, Oct. 1990.

[87] Y. Freund and R. E. Schapire, "Large margin classification using the perceptron algorithm," *Mach. Learn.*, vol. 37, no. 3, pp. 277–296, 1999.

[88] C. J. Tucker, "Red and photographic infrared linear combinations for monitoring vegetation," *Remote Sens. Environ.*, vol. 8, no. 2, pp. 127–150, 1979.

[89] A. Huete, K. Didan, T. Miura, E. P. Rodriguez, X. Gao, and L. G. Ferreira, "Overview of the radiometric and biophysical performance of the MODIS vegetation indices," *Remote Sens. Environ.*, vol. 83, no. 1–2, pp. 195–213, 2002.

[90] J. G. Qi, A. R. Chehbouni, A. R. Huete, Y. H. Kerr, and S. Sorooshian, "A modified soil adjusted vegetation index," *Remote Sens. Environ.*, vol. 48, no. 2, pp. 119–126, 1994.

[91] A. A. Gitelson, Y. Zur, O. B. Chivkunova, and M. N. Merzlyak, "Assessing carotenoid content in plant leaves with reflectance spectroscopy," *Photochem. Photobiol.*, vol. 75, no. 3, pp. 272–281, 2010.

[92] A. A. Gitelson, M. N. Merzlyak, and O. B. Chivkunova, "Optical properties and nondestructive estimation of anthocyanin content in plant leaves," *Photochem. Photobiol.*, vol. 74, no. 1, pp. 38–45, 2010.

[93] B. Datt, "A new reflectance index for remote sensing of chlorophyll content in higher plants: Tests using eucalyptus leaves," *J. Plant Physiol.*, vol. 154, no. 1, pp. 30–36, 1999.

[94] D. A. Sims and J. A. Gamon, "Relationships between leaf pigment content and spectral reflectance across a wide range of species, leaf structures and developmental stages," *Remote Sens. Environ.*, vol. 81, no. 2–3, pp. 337–354, 2002.

[95] W. J. Frampton, J. Dash, G. Watmough, and E. J. Milton, "Evaluating the capabilities of Sentinel-2 for quantitative estimation of biophysical variables in vegetation," *ISPRS-J. Photogramm. Remote Sens.*, vol. 82, pp. 83–92, 2013.

[96] N. H. Broge and E. Leblanc, "Comparing prediction power and stability of broadband and hyperspectral vegetation indices for estimation of green leaf area index and canopy chlorophyll density," *Remote Sens. Environ.*, vol. 76, no. 2, pp. 156–172, 2001.

[97] J. Dash and P. J. Curran, "The MERIS terrestrial chlorophyll index," *Int. J. Remote Sens.*, vol. 25, no. 23, pp. 5403–5413, 2004.

[98] A. A. Gitelson, Y. Gritz, and M. N. Merzlyak, "Relationships between leaf chlorophyll content and spectral reflectance and algorithms for non-destructive chlorophyll assessment in higher plant leaves," *J. Plant Physiol.*, vol. 160, no. 3, pp. 271–282, 2003.

[99] C. S. T. Daughtry, C. L. Walthall, M. S. Kim, E. B. D. Colstoun, and M. M. Iii, "Estimating corn leaf chlorophyll concentration from leaf and canopy reflectance," *Remote Sens. Environ.*, vol. 74, no. 2, pp. 229–239, 2000.

[100] P. J. Curran, W. R. Windham, and H. L. Gholz, "Exploring the relationship between reflectance red edge and chlorophyll concentration in slash pine leaves," *Tree Physiol.*, vol. 15, no. 3, pp. 203–206, 1995.

[101] D. Haboudane, J. R. Miller, E. Pattey, P. J. Zarco-Tejada, and I. B. Strachan, "Hyperspectral vegetation indices and novel algorithms for predicting green LAI of crop canopies: Modeling and validation in the context of precision agriculture," *Remote Sens. Environ.*, vol. 90, no. 3, pp. 337–352, 2004.

[102] L. Gao, X. Wang, B. A. Johnson, Q. Tian, Y. Wang, and J. Verrelst, "Remote sensing algorithms for estimation of fractional vegetation cover using pure vegetation index values: A review," *ISPRS-J. Photogramm. Remote Sens.*, vol. 159, pp. 364–377, 2020.

[103] X. Dai, Z. Huo, and H. Wang, "Simulation for response of crop yield to soil moisture and salinity with artificial neural network," *Field Crops Res*, vol. 121, no. 3, pp. 441–449, 2011.

[104] D. J. Lary, A. H. Alavi, A. H. Gandomi, and A. L. Walker, "Machine learning in geosciences and remote sensing," *Geosci. Frontiers*, vol. 7, no. 1, pp. 3–10, 2016.

[105] Z. Yufang, G. Jianya, S. Kun, Y. Jianmin, and C. Xiaoling, "Estimation of soil moisture index using multi-temporal Sentinel-1 images over poyang lake ungauged zone," *Remote Sens.*, vol. 10, no. 1, 2017, Art. no. 12.

[106] L. Zhiqu, L. Pingxiang, and Y. Jie, "Soil moisture retrieval and spatiotemporal pattern analysis using Sentinel-1 data of Dahra," *Remote Sens.*, vol. 9, no. 11, 2017, Art. no. 1197.

[107] A. Amazirh, O. Merlin, S. Er Raki, Q. Gao, V. Rivalland, and Y. Malbeteau, "Retrieving surface soil moisture at high spatio-temporal resolution from a synergy between Sentinel-1 radar and Landsat thermal data: A study case over bare soil," *Remote Sens. Environ.*, vol. 211, pp. 321–337, 2018.

[108] A. Reza, A. Jalal, N. Claudia, and G. Felix, "Synergetic use of Sentinel-1 and Sentinel-2 data for soil moisture mapping at plot scale," *Remote Sens.*, vol. 10, no. 8, 2018, Art. no. 1285.

[109] J. Ezzahar, N. Ouaadi, M. Zribi, J. Elfarkh, and L. Jarlan, "Evaluation of backscattering models and support vector machine for the retrieval of bare soil moisture from Sentinel-1 data," *Remote Sens.*, vol. 12, no. 1, 2019, Art. no. 72.

[110] S. Huang, J. Ding, J. Zou, B. Liu, J. Zhang, and W. Chen, "Soil moisture retrieval based on Sentinel-1 imagery under sparse vegetation coverage," *Sensors*, vol. 19, no. 3, 2019, Art. no. 589.

[111] B. Safa, Z. Mehrez, L. C. Zohra, B. Nicolas, E. H. Mohammad, and G. Qi, "Potential of Sentinel-1 radar data for the assessment of soil and cereal cover parameters," *Sensors*, vol. 17, no. 11, 2017, Art. no. 2617.
[112] A. Sekertekin, A. M. Marangoz, and S. Abdikan, "ALOS-2 and Sentinel-1 SAR data sensitivity analysis to surface soil moisture over bare and vegetated agricultural fields," *Comput. Electron. Agriculture*, vol. 171, pp. 1–11, 2020.
[113] S. Bousbih, M. Zribi, M. El Hajj, N. Baghdadi, Z. Lili-Chabaane, and Q. Gao, "Soil moisture and irrigation mapping in a semi-arid region, based on the synergetic use of Sentinel-1 and Sentinel-2 data," *Remote Sens.*, vol. 10, no. 12, 2018, Art. no. 1953.
[114] A. Singh, K. Gaurav, G. K. Meena, and S. Kumar, "Estimation of soil moisture applying modified dubois model to Sentinel-1; a regional study from central India," *Remote Sens.*, vol. 12, no. 14, pp. 1–19, 2020.
[115] D. Z. Katarzyna, B. Maria, T. Monika, M. Alicja, G. Martyna, and B. Maciej, "Assessment of carbon flux and soil moisture in wetlands applying Sentinel-1 data," *Remote Sens.*, vol. 8, no. 9, 2016, Art. no. 756.
[116] D. D. Alexakis, F. K. Mexis, A. K. Vozinaki, I. N. Daliakopoulos, and I. K. Tsanis, "Soil moisture content estimation based on Sentinel-1 and auxiliary earth observation products. A hydrological approach," *Sensors*, vol. 17, no. 6, 2017, Art. no. 1455.
[117] K. Dabrowska Zielinska, J. Musial, A. Malinska, M. Budzynska, and P. Grzybowski, "Soil moisture in the biebrza wetlands retrieved from Sentinel-1 imagery," *Remote Sens.*, vol. 10, no. 12, 2018, Art. no. 1979.
[118] H. J. F. Benninga, R. V. D. Velde, and Z. Su, "Impacts of radiometric uncertainty and weather-related surface conditions on soil moisture retrievals with Sentinel-1," *Remote Sens.*, vol. 11, no. 17, 2019, Art. no. 2025.
[119] A. Hachani, M. Ouessar, S. Paloscia, E. Santi, and S. Pettinato, "Soil moisture retrieval from Sentinel-1 acquisitions in an arid environment in Tunisia: Application of artificial neural networks techniques," *Int. J. Remote Sens.*, vol. 40, no. 24, pp. 9159–9180, 2019.
[120] W. Zhuo, J. Huang, L. Li, X. Zhang, and X. Xiao, "Assimilating soil moisture retrieved from Sentinel-1 and Sentinel-2 data into WOFOST model to improve winter wheat yield estimation," *Remote Sens.*, vol. 11, no. 11, 2019, Art. no. 1618.
[121] C. D. K. Ma, W. N. Yang, and C. Ma, "Estimation of soil moisture in time-series dual-polarization SAR mining subsidence area," *J. Remote Sens.*, vol. 22, no. 3, pp. 521–534, 2018.
[122] A. Tripathi and R. K. Tiwari, "Synergetic utilization of Sentinel-1 SAR and Sentinel-2 optical remote sensing data for surface soil moisture estimation for Rupnagar, Punjab, India," *Geocarto Int.*, vol. Apr. 2020, pp. 1–22, 2020.
[123] M. Hosseini and H. McNairn, "Using multi-polarization C- and L-band synthetic aperture radar to estimate biomass and soil moisture of wheat fields," *Int. J. Appl. Earth Observ. Geoinf.*, vol. 58, pp. 50–64, 2017.
[124] B. Xiaojing, H. Binbin, L. Xing, Z. Jiangyuan, W. Xin, and W. Zuoliang, "First assessment of Sentinel-1A data for surface soil moisture estimations using a coupled water cloud model and advanced integral equation model over the tibetan plateau," *Remote Sens.*, vol. 9, no. 7, 2017, Art. no. 714.
[125] N. Guindin-Garcia, A. A. Gitelson, T. J. Arkebauer, J. Shanahan, and A. Weiss, "An evaluation of MODIS 8- and 16-day composite products for monitoring maize green leaf area index," *Agricultural Forest Meteorol.*, vol. 161, pp. 15–25, 2012.
[126] A. Mercier, J. Betbeder, J. Baudry, J. Denize, and L. Hubert-Moy, "Evaluation of Sentinel-1 and -2 time series to derive crop phenology and biomass of wheat and rapeseed: Northen france and brittany case studies," in *Proc. Remote Sens. Agriculture, Ecosyst., Hydrol. XXI*, vol. 11149, 2019, Art. no. 1114903.
[127] M. E. Hajj, N. Baghdadi, H. Bazzi, and M. Zribi, "Penetration analysis of SAR signals in the C and L bands for wheat, maize, and grasslands," *Remote Sens.*, vol. 11, no. 1, 2018, Art. no. 31.
[128] M. Xing, B. He, X. Ni, J. Wang, and X. Huang, "Retrieving surface soil moisture over wheat and soybean fields during growing season using modified water cloud model from Radarsat-2 SAR data," *Remote Sens.*, vol. 11, no. 16, 2019, Art. no. 1956.
[129] P. Kumar, R. Prasad, A. Choudhary, D. K. Gupta, and V. N. Mishra, "Comprehensive evaluation of soil moisture retrieval models under different crop cover types using C-band synthetic aperture radar data," *Geocarto Int.*, vol. 34, no. 9, pp. 1022–1041, 2019.
[130] P. Ramendra, R. C. Deo, L. Yan, and M. Tek, "Soil moisture forecasting by a hybrid machine learning technique: ELM integrated with ensemble empirical mode decomposition," *Geoderma*, vol. 330, pp. 136–161, 2018.
[131] Y. Ban, P. Zhang, A. Nascetti, A. R. Bevington, and M. A. Wulder, "Near real-time wildfire progression monitoring with Sentinel-1 SAR time series and deep learning," *Sci. Rep.*, vol. 10, no. 1, 2020, Art. no. 1322.
[132] G. Tayfur, G. Zucco, L. Brocca, and T. Moramarco, "Coupling soil moisture and precipitation observations for predicting hourly runoff at small catchment scale," *J. Hydrol.*, vol. 510, no. 6, pp. 363–371, 2014.
[133] Y. Cui, C. Zeng, J. Zhou, H. Xie, and Y. Hong, "A spatio-temporal continuous soil moisture dataset over the Tibet plateau from 2002 to 2015," *Sci. Data*, vol. 6, no. 1, 2019, Art. no. 247.
[134] K. O. Achieng, "Modelling of soil moisture retention curve using machine learning techniques: Artificial and deep neural networks vs support vector regression models," *Comput. Geosci.*, vol. 133, 2019, Art. no. 104320.
[135] C. Evangelides and A. Nobajas, "Red-edge normalised difference vegetation index (NDVI705) from Sentinel-2 imagery to assess post-fire regeneration," *Remote Sens. Appl. Soc. Environ.*, vol. 17, 2020, Art. no. 100283.
[136] H. T. M. Dinh, D. Ienco, R. Gaetano, N. Lalande, and E. Ndikumana, "Deep recurrent neural networks for mapping winter vegetation quality coverage via multi-temporal SAR Sentinel-1," *IEEE Geosci. Remote Sens. Lett.*, vol. 15, no. 3, pp. 464–468, Mar. 2018.
[137] L. Zhang, L. Zhang, and B. Du, "Deep learning for remote sensing data: A technical tutorial on the state-of-the-art," *IEEE Geosci. Remote Sens. Mag.*, vol. 4, no. 2, pp. 22–40, Jun. 2016.
[138] X. Zhu, D. Tuia, L. Mou, G. S. Xia, L. Zhang, and F. Xu, "Deep learning in remote sensing: A comprehensive review and list of resources," *IEEE Geosci. Remote Sens. Mag.*, vol. 5, no. 4, pp. 8–36, Dec. 2018.
[139] L. Ma, Y. Liu, X. Zhang, Y. Ye, G. Yin, and B. A. Johnson, "Deep learning in remote sensing applications: A meta-analysis and review," *ISPRS-J. Photogramm. Remote Sens.*, vol. 152, pp. 166–177, 2019.

Ying Liu received the Ph.D. degree in photogrammetry and remote sensing from China University of Mining and Technology, Beijing, China, in 2013.

She is currently an Associate Professor with Xi'an University of Science and Technology, Xi'an, China. Her research interests include remote sensing monitoring of mine environment (multisource remote sensing and cooperative observation), remote sensing inversion of soil moisture (drought monitoring and drought prediction), and quantitative remote sensing (information extraction and spatial–temporal analysis of remote sensing data).

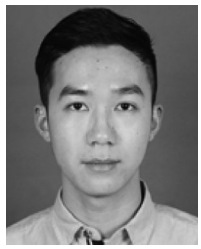

Jiaxin Qian received the B.S. degree in remote sensing science and technology from Nanjing University of Information Science and Technology, Nanjing, China, in 2018. He is currently working toward the M.S. degree in surveying engineering at Xi'an University of Science and Technology, Xi'an, China.

His research interest includes inversion of soil moisture and terrain deformation by optical and SAR images.

Hui Yue received the Ph.D. degree in environmental sciences from China University of Mining and Technology, Beijing, China, in 2013.

He is currently a Lecturer with Xi'an University of Science and Technology, Xi'an, China. His research interests include remote sensing of environment, extraction of remote sensing geoscience information, and monitoring and assessment of ecological environment.